Design of a Field-Intensified Interior Permanent Magnet Synchronous Machine for Electric Vehicle Application

by

Michiel Hendrik Albertus Prins

Thesis presented in fulfilment of the requirements for the degree
Master of Science in Electrical and Electronic Engineering
at the University of Stellenbosch

Supervisor:
Prof. Maarten J. Kamper, University of Stellenbosch

Maart 2014

Declaration

By submitting this thesis electronically, I declare that the entirety of the work contained therein is my own, original work, that I am the owner of the copyright thereof (unless to the extent explicitly otherwise stated), and that I have not previously in its entirety or in part submitted it for obtaining any qualification.

Date: December 2013

Abstract

The focus of this thesis is on the optimal design and evaluation of FI-PM machines to be used with a MG transmission drive-train for EV application.

The machines presented are optimised using a gradient-based optimisation algorithm of the VisualDoc software together with FE software and Python scripts. Each machine is optimised for its own objective function. The focus is to reduce expensive rare earth material.

High torque ripple issues of the optimised machines are solved by implementing a relatively new topology where the rotor poles/barriers are made asymmetric. The asymmetric rotor topology implemented is effective and can be used as an alternative for rotor stack skewing.

PM demagnetisation and rotor deformation studies are conducted on the optimum designed machines to ensure that no PM demagnetisation on the surface of the PMs and critical rotor deformation occur.

The FE performance results of the optimum designed machines are shown and discussed. One of the optimum designed FI-PM machines is manufactured and tested in the laboratory. The FE and measured results of the machine are compared and shows good correlation.

The saliency performance of the optimum designed machines are evaluated as it determines its position sensorless control capability. It is shown that the saliency ratios increase linearly with load, making it favourable for position sensorless control. It is also shown that the asymmetric rotor topologies introduced a larger mutual inductance compared to their symmetric counterparts, thus higher cross-coupling is present in these rotors and therefore a higher saliency shift, which is undesirable. Two case studies are performed in order to improve saliency performance. The objective of the first case study is to improve the saliency shift by reducing the flux leakage paths in the rotor. The objective of the second case study is to optimise a FI-PM machine in order to improve the saliency ratio and -shift. The results of the two case studies are compared with the saliency performance of the other machines.

Uittreksel

Die fokus van hierdie tesis is op die optimale ontwerp en evaluering van veld versterking permanente magneet masjiene vir veelvoudige-rat elektriese voertuig toepassings.

Die masjiene teenwoordig is geoptimeer met behulp van 'n helling-gebaseerde optimering algoritme. Elke masjien is geoptimeer vir sy eie doel funksie. Die fokus is om duur seldsame permanent magneet materiaal te verminder.

Hoë wringkrag-rimpeleffek van die optimale masjiene word opgelos deur die implementering van 'n relatief nuwe topologie waar die rotor pole/vloedbarrière asimmetries gemaak word. Die asimmetriese rotor topologie wat geimplementeer is, is effektief en kan dus as 'n alternatief vir die rotor stapel skeef metode gebruik word.

Permanent magneet demagnetisering en rotor vervorming studies is ook uitgevoer op die optimum ontwerpte masjiene om te verseker dat geen demagnetisering plaasvind nie en ook geen kritiese rotor vervorming nie.

Die eindige-element resultate van die optimum ontwerpte masjiene word getoon en bespreek. Een van die optimum ontwerpte veld versterking permanente magneet masjiene is vervaardig en getoets in die laboratorium . Die eindige-element en gemete resultate van die masjien word vergelyk en toon goeie korrelasie.

Die speek prestasie van die optimum ontwerpte masjiene word geëvalueer aangesien dit die sensorlose posisie beheer vermoë bepaal. Daar word getoon dat die speek koëffisiënt verhoog lineêr met vrag wat dit gunstig maak vir posisie sensorlose beheer . Daar word ook gewys dat die asimmetriese rotor topologie 'n groter wedersydse induktansie het in vergelyking met hul simmetriese eweknieë, dus is daar hoër kruis-koppeling teenwoordig in die rotors en dus 'n hoër speek skuif, wat ongewens is. Twee gevallestudies om speek prestasie te verbeter is uitgevoer. Die doel van die eerste gevallestudie is om die speek skuif te verbeter deur die vermindering van die vloed lekkasie paaie in die rotor. Die doel van die tweede gevallestudie is om 'n veld versterking permanente magneet masjiene te optimeer ten einde die speek koëffisiënt en - skuif te verbeter. Die resultate van die twee gevallestudies word vergelyk met die speek prestasie van die ander masjiene.

Acknowledgements

I would like to express my sincere appreciation to:

- My heavenly Father and Saviour, for His endless love and blessings.
- Prof. Maarten Kamper, my promoter, for his supervision, support and his efforts to ensure the availability of financial resources.
- The international office of the University of Stellenbosch, for financial support.
- Wikus Villet and David Groenewald for implementation of the control scheme and help with lab tests.
- Andre Swart, Murry Jumat and Petro Petzer for the mechanical support setting up the test benches etc.
- My family who supported me throughout this thesis and for their interest by always enquiring how the work is progressing.
- Laryssa Theron, the love of my life, for your loving support and encouragement.

Nomenclature

Acronyms

BR-FI-PM	Basic Rotor Flux Intensified Permanent Magnet
CPSR	Constant Power Speed Range
DSP	Digital Signal Processor
EV	Electric Vehicle
FBR-FI-PM	Flux Barrier Rotor Field Intensified Permanent Magnet
FE	Finite Element
FG	Fixed Gear
FI	Field Intensifying
FI-PM	Field Intensified Permanent Magnet
FW	Field Weakening
FW-IPM	Field Weakening Interior Permanent Magnet
ICE	Internal Combustion Engine
IPM	Interior Permanent Magnet
MG	Multi-Gear
MMFD	Modified Method of Feasible Direction
SIPM	Segmented Interior Permanent Magnet
SLP	Sequential Linear Programming
SQP	Sequential Quadratic Programming
SUMT	Sequential Unconstrained Minimisation Technique
THD	Total Harmonic Distortion

Roman Symbols

A	magnetic vector potential	[Wb.m^{-1}]
A_{cu}	active copper area per slot	[m^2]
A_s	stator coil area	[m^2]
b_p	barrier pitch	[°]
b_w	barrier width	[mm]

B	magnetic flux density magnitude	[Tesla]
d_r	rotor outer diameter	[m]
d_{si}	stator-bore inner diameter	[mm]
G_r	rotor mass	[kg]
ℓ_e	end-winding length	[mm]
ℓ_g	air-gap length	[mm]
ℓ_s	active stack length	[mm]
I	phase current magnitude [A]	
J	current density magnitude	[A.mm^{-2}]
k_{dv}	distribution factor at harmonic order ν	
k_{pv}	pitch factor at harmonic order ν	
k_{wv}	winding factor at harmonic order ν	
L	inductance	[Henry]
L_e	end-winding inductance	[Henry]
m_h	magnet height	[mm]
m_w	magnet width	[mm]
n	mechanical rotor speed	[r/min]
n_a	number of parallel circuits of the stator winding	
N	number of turns in series per phase	
p	pole pairs	
pp	pole pitch	[mm]
P_{cu}	copper loss	[kW]
P_e	eddy-current loss	[W]
P_{fe}	iron losses	[W]
P_h	hysteresis loss	[W]
P_{rot}	mechanical rotational losses	[W]
q	slots per pole phase group	
r	radius	[m]
ro_{id}	rotor inner diameter	[mm]
ro_{od}	rotor outer diameter	[mm]
r_s	phase winding resistance	[Ω]

$slot_h$	slot height	[mm]
st_{od}	stator outer diameter	[mm]
t	temperature	[$^\circ C$]
$t\_i\_b_w$	top inner barrier width	[mm]
$t\_m\_b_w$	top middle barrier width	[mm]
t_w	tooth width	[mm]
T_{avg}	average torque	[Nm]
T_{em}	electromagnetic torque	[Nm]
T_{inst}	instantaneous torque	[Nm]
T_{rip}	torque ripple	[%]
V_e	volume of a mesh element	[m^3]
V_{pm}	permanent magnet volume	[cm^3]
w	coil-span pitch	[°]
W	number of turns in series per phase	
x_p	vertex of the parabola	[mm]
$X_1,\, X_2 \ldots X_n$	individual design variables	
y_h	yoke height	[mm]
z	number of turns per slot	

Greek Symbols

α	step size	
α_b	coefficient of the magnetic flux density	
α_u	slot pitch	[$^\circ e$]
γ	angle between the current and flux linkage space phasors	[$^\circ e$]
Γ	contour in centre of air-gap	
η	efficiency	[%]
θ_e	electrical rotor position	[$^\circ e$]
λ_a	phase a flux linkage	[Vs]
λ_e	end-winding flux linkage	[Vs]
λ_g	stator winding air-gap flux linkage	[Vs]

λ_l	leakage flux linkage	[Vs]
λ_{PM}	permanent magnet flux linkage	[Vs]
μ_0	permeability of free space	[Vs.Am^{-1}]
ν	harmonic order	
ρ	resistivity	[Ωm]
τ_p	pole pitch	[°]
ϕ	current space phasor angle	[$^\circ e$]
ω_e	electrical rotor velocity	[rad/s]

Phasors, vectors and matrices

$\mathbf{F}$	objective function
$\boldsymbol{g}$	vector containing the inequality constraints
$\boldsymbol{h}$	vector containing the equality constraints
$\boldsymbol{i}_{abc}$	3-phase stator current vector
$\boldsymbol{i}_{dq0}$	stator current vector in the dq0 reference frame
$\boldsymbol{I}_{dqo}$	steady-state stator current vector in the $dq0$ reference frame
$\boldsymbol{I_s}$	stator current space phasor
$\boldsymbol{k}_p$	Park's transformation matrix
$\mathbf{u}$	vector containing the equality constraints
$\boldsymbol{v}_{dq0}$	stator voltage vector in the dq0 reference frame
$\boldsymbol{V}_{dq0}$	steady-state stator voltage vector in the dq0 reference frame
$\mathbf{X}$	multi-dimensional vector containing the design variables
$\mathbf{X}_L$, $\mathbf{X}_U$	lower and upper side constraint vectors
$\boldsymbol{\lambda}_{abc}$	3-phase stator winding flux linkage vector
$\boldsymbol{\lambda}_{dqo}$	stator winding air-gap flux linkage vector in the $dq0$ reference frame
$\boldsymbol{\lambda_s}$	stator flux linkage space phasor
$\boldsymbol{v}_{abc}$	3-phase stator voltage vector

Indices and Subscripts

d	d-axis in the $dq0$ reference frame
e	electrical
q	q-axis in the $dq0$ reference frame

Contents

1 Introduction 1

1.1 Description of FI-PM machine 1

1.2 History of FI-PM machine 2

1.3 Application: EV Drive-train 4

1.4 Design specification 7

1.5 Objectives and thesis layout 8

2 Mathematical Modelling of the FI-IPM machine 9

2.1 Equivalent circuit model 9

2.2 Calculation of equivalent dq circuit parameters 11

2.2.1 Phase resistance 11

2.2.2 dq currents 12

2.2.3 Flux linkage 12

2.2.3.1 Air gap flux linkage 12

2.2.3.2 End-winding leakage flux 14

2.2.4 dq voltages 14

2.3 Torque 15

2.4 Efficiency 16

3 FE Design Optimisation 18

3.1 Optimisation theory 18

3.1.1 Constrained optimisation algorithms 18

3.1.2 Optimisation process 19

3.2 FI-PM machine optimisation 22

3.2.1 Pre-optimisation discussion . . . 23
3.2.2 Design optimisation of Basic Rotor FI-PM machine . . . 24
3.2.3 FI-PM machine with internal flux barriers optimisation . . . 27
3.2.4 Asymmetric rotor configuration . . . 30
3.2.4.1 Asymmetric BR-FI-PM machine . . . 31
3.2.4.2 Asymmetric FBR-FI-PM machine . . . 32
3.3 Summary . . . 33

4 PM demagnetisation and rotor deformation 34
4.1 PM demagnetisation . . . 34
4.2 Rotor deformation . . . 37
4.3 Summary . . . 38

5 FE and measured results 39
5.1 FE results of optimum designed machines . . . 39
5.2 Measured Results . . . 42
5.2.1 Experimental setup . . . 43
5.2.2 Open-circuit . . . 43
5.2.3 Load . . . 44
5.3 Summary . . . 45

6 Saliency Performance of the FI-PM machine 48
6.1 Saliency ratio and -shift . . . 48
6.2 Saliency performance comparison . . . 49
6.3 Summary . . . 52

7 Conclusions 53
7.1 Design optimisation . . . 53
7.2 PM demagnetisation and rotor deformation . . . 54
7.3 Optimum designed machines . . . 54
7.4 Saliency performance . . . 54
7.5 Recommendations for future work . . . 55

References 56

List of Tables

1.1 Design specifications of electric traction machine 7

3.1 Winding factors calculated for different chording ratios. 24

3.2 Optimum design variables obtained from the optimisation for the BR-FI-PM machine. 26

3.3 $\frac{P_{cu}}{T}$ as a function of ℓ_s. 29

3.4 Optimum design variables obtained from the optimisation for the FBR-FI-PM machine. 30

3.5 Optimum barrier pitches obtained from the optimisation for the FBR-FI-PM machine optimised for minimum torque ripple. 30

3.6 Optimum PM widths found from the optimisation for the asymmetric BR-FI-PM machine. 32

3.7 Optimum flux barrier pitches found from the optimisation for the asymmetric FBR-FI-PM machine. 33

4.1 Conditions 35

5.1 FE performance results of the optimised machines. 41

List of Figures

1.1 (a) FI-PM machine topology. (b)FW-IPM machine topology. 2
1.2 Spectrum of EV drives. 4
1.3 Tractive effort of ICE with MG transmission. 5
1.4 Tractive effort of the Opel Corsa 1.4i Lite vehicle with 5-speed MG transmission. 6
1.5 Torque-speed graphs for different FG ratios. 6

2.1 Steady-state d- and q-axis equivalent circuits of the FI-PM machine. 11
2.2 Space phasor diagram fixed in the rotating rotor reference frame. 13

3.1 Local and global minimums. 19
3.2 Optimisation process flowchart. 22
3.3 Quarter cross-section of the BR-FI-PM machine showing the rotor design variables. The stator variables are fixed and are not shown. 25
3.4 (a) Quarter cross-section showing the design variables of the FBR-FI-PM machine. (b) An enlarged section of the quarter cross-section showing the iron ribs. 27
3.5 Half cross-section showing the design variables of the asymetric BR-FI-PM machine. 31
3.6 Half cross-section showing the design variables of the asymetric FBR-FI-PM machine. 32

4.1 armature reaction effect. 35
4.2 Quarter cross-sections showing the demagnetisation ratio for (a) the BR-FI-PM machine and (b) the FBR-FI-PM machine for the conditions in Table 4.1. . . . 36

4.3 Cut-out sections showing signs of demagnetisation on the surface of the PMs for (a) the BR-FI-PM machine and (b) the FBR-FI-PM machine. 36
4.4 Quarter cross-section of the BR-FI-PM machine's rotor showing (a) the deformation and (b) the deformation scaled by one hundred, at 4800 r/min speed. . 37
4.5 Quarter cross-section of the FBR-FI-PM machine's rotor showing (a) the deformation and (b) the deformation scaled by one hundred, at 4800 r/min speed. 38

5.1 Quarter cross-sections of (a) BR-FI-PM,(b) asymmetric BR-FI-PM, (e) FBR-FI-PM and (f) asymmetric FBR-FI-PM machines, and their field plots in (c), (d), (g) and (h) respectively. 40
5.2 Torque as a function of rotor position of the FI-PM machines at full load. . . . 42
5.3 Full-load torque harmonics of the FI-PM machines. 42
5.4 Efficiency map for (a) asymmetric BR-FI-PM and (b) asymmetric FBR-FI-PM. 43
5.5 Diagram of the test setup. 44
5.6 Pictures of the test bench setup and machine components. 45
5.7 (a) Measured and calculated open-circuit rms phase voltage. (b) Measured open-circuit phase voltage waveforms at 156.25 Hz (4687.5 r/min). 46
5.8 Measured and FE calculated torque. 46
5.9 Measured and FE calculated current according to the load torque in Fig. 5.8. . 47
5.10 Measured and FE calculated efficiency according to the load torque in Fig. 5.8. 47

6.1 (a) FE calculated saliency ratio. (b) FE calculated saliency shift. 50
6.2 Mutual inductances. 51
6.3 The FI-PM machine of case study 1. 51

Chapter 1

Introduction

1.1 Description of FI-PM machine

The Field Intensified Permanent Magnet (FI-PM) machine is a relatively new type of machine, therefore, a short explanation of the topology is given here for a good understanding of the machine.

The easiest way to realise a FI-PM machine is by adding q-axis flux barriers to obstruct the q-axis flux paths so that $L_d > L_q$, shown in Fig. 1.1a. The Permanent Magnet (PM) is situated on the d-axis and therefore its height must not be greater than the combined height of the q-axis flux barriers in order to keep $L_d > L_q$. With $L_d > L_q$ a positive d-axis current I_d is required (or Field-Intensified FI current) rather than the classical negative I_d for Field Weakening Interior Permanent Magnet (FW-IPM) machines, shown in Fig. 1.1b. This is a big advantage over classical FW-IPM machines since the positive I_d assist the PM flux instead of opposing it, therefore, reducing the risk of PM demagnetisation and thinner magnets can be used, thus reducing cost. Initially the FI-PM machine operates with positive I_d to benefit from the reluctance torque. As the speed increases and the voltage limit is reached, the positive I_d need to be reduced by advancing the current space phasor angle so that I_d eventually becomes negative (FW current) to further suppress the voltage. The current space phasor is defined by $\boldsymbol{I}_s = I\angle\phi = I_d + jI_q$. Only a small amount of negative I_d is needed above rated speed to obtain good FW capabilities [1]. Another advantage of FI-PM machines is that the saliency do not disappear under load conditions as I_q increases. This can be explained by the q-axis flux paths which saturates as I_q increases with load which causes L_q to decrease. Due to

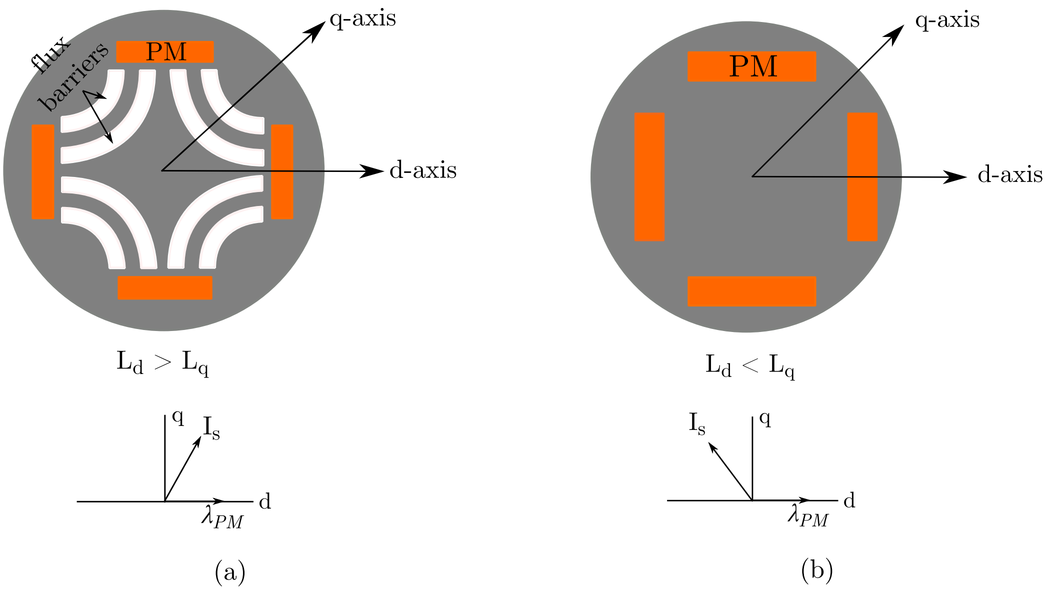

Figure 1.1: (a) FI-PM machine topology. (b)FW-IPM machine topology.

$L_d > L_q$ the difference between the two inductances become larger as the load increases, thus, causing the saliency to increase. The saliency is much more linear, due to less saturation effects, than in FW-IPM machines which is advantageous for sensorless control [1].

1.2 History of FI-PM machine

The FI-PM machine is a relatively new type of electrical machine first introduced in 1999 by *Nicola Bianchi* who named it the Segmented Interior Permanent Magnet (SIPM) motor. Flux barriers was added in the rotor to obstruct q-axis flux paths so that $L_d > L_q$ which is the most recognised property of the FI-PM machine, rather than $L_d < L_q$ like in conventional FW-IPM machines. This was done to achieve higher torque capabilities above rated speed i.e. in the FW operating region [2]. In 2000, another article was published by the same author on this work [3]. After these two publications the FI-PM machines didn't receive much attention and it was only in 2006 when it appeared in literature again.

The main concern in 2006 was to design a cost effective machine but still maintain a high power density, hence, a machine with low PM volume since rare earth PM's are expensive due to the limited supply chain. Since a large negative d-axis current is needed above rated speed in FW-IPM's, a thin or small magnet cannot be used due to the risk of demagnetisation. Thus, a FI-PM is proposed which utilises a small amount of d-axis current above rated speed, therefore, reducing the risk of PM demagnetisation and thinner or smaller PM's can be used. A key technique to reduce PM volume is to utilise more reluctance torque which is generated by the saliency of the machine [4]. The saliency can be increased by strategic placement of the flux barriers in the rotor.

In 2009 a FI-PM machine was designed to improve the sensorless capabilities of the machine especially at low speed. The aim was to reduce saturation induced saliency, cross-coupling effects and also secondary saliencies which reduces the estimation accuracy of sensorless control schemes since it reduces the saliency ratio. This was achieved by adding flux barriers across the q-axis and changing the position of the PM's [5]. The influence of the rotor geometry on sensorless control for IPM's are discussed in [6] and design hints are given in [7] which is also applicable on FI-PM machines. In 2010 a study of FI-PM machines with distributed and concentrated windings were conducted. The effects of the two winding configurations on the sensorless control performance were investigated. It was found that the concentrated winding design produced more saliency which could improve the sensorless control performance, however, these designs have higher secondary saliencies which contribute to an increase in the position estimation error due to an increase in THD [8].

A new rotor design was proposed in 2011 for a FI-PM machine that is more suitable for sensorless control at zero/very-low speed. The proposed FI-PM machine showed less variation in L_d and L_q when the machine is loaded, therefore, leading to the possibility of better sensorless control at zero/very-low speed compared to the conventional FW-IPM machine [1]. In 2012 the focus was to reduce expensive rare earth materials even more by using low coercive force magnets[1] with magnetisation level control. The machine was called the variable MMF FI-PM machine due to the fact that the magnetising state of the magnets can be controlled. It was found that the magnetisation state of the magnets remained stable under loaded and even overload conditions. The machine was able to achieve a wide torque-speed envelope with the low coercive force magnets [9, 10]. In 2013 the sensorless control capability of a FI-PM machine was investigated using several sensorless control methods. The FI-PM machine showed good sensorless capabilities with good estimation accuracy for all the methods [11].

---

[1] Low coercive force magnets do not include expensive rare earth materials like dysprosium [9].

1.3 Application: EV Drive-train

FI-PM machines are designed and optimised for a Multi-Gear (MG) Electric Vehicle (EV) application. The design specifications are according to the tractive effort and power specification of a Internal Combustion Engine (ICE) powered Opel Corsa. The standard clutch and 5-speed manual transmission with differential of the Opel Corsa are used for the investigation.

In the spectrum of EV drives research focuses on direct in-wheel (hub) drives on the one side to Fixed Gear (FG) plus differential single-electric motor drives on the other side of the spectrum, shown in Fig. 1.2. A further step in this spectrum is to use the MG plus differential electric drive-train, similar to what is used in ICE powered vehicles. MG electric drive-trains for EVs receive almost no attention in literature. It is only recently that studies are directed towards MG electric drive-trains for EV's [12–16].

The torque-speed characteristics are shown in Fig. 1.3 for a typical ICE (solid lines) and a ideal ICE (dotted line). ICE's have a relatively flat torque-speed profile as compared with

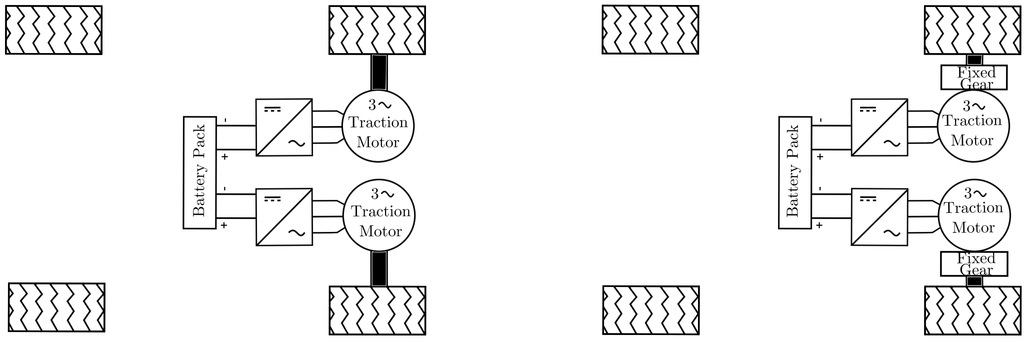

(a) Direct in-wheel drive. (b) In-wheel with fixed-gear drive.

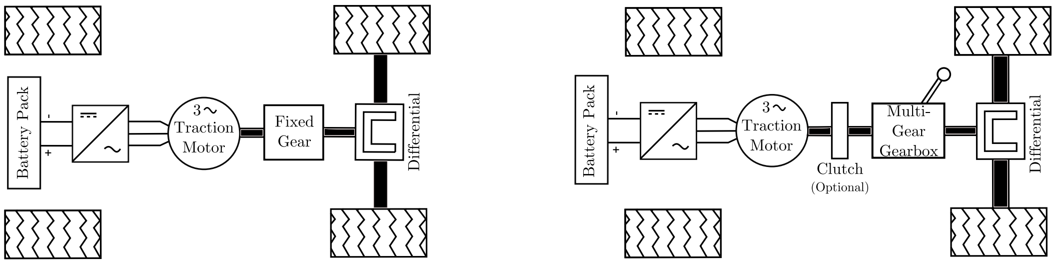

(c) Fixed-gear with differential drive. (d) Multiple-gear with differential drive.

Figure 1.2: Spectrum of EV drives.

an ideal ICE, therefore, MG transmissions are employed to modify the profile so that it approaches the ideal as shown in Fig. 1.3. The ideal torque-speed characteristics of the MG ICE powered vehicle match perfectly with the torque-speed characteristics of a FG electric motor drive system in FW mode [17, 18]. Hence, single electric motor EV drives are usually implemented with FG transmissions. However, with FG EV drive-trains the power performance of the vehicle strongly depends on the FW performance or the Constant Power Speed Ratio (CPSR) of the electric drive.

In order to meet the tractive effort specifications of each gear of the ICE as shown in Fig. 1.4, with a FG EV drive-train, a very high speed motor is needed compared to a drive-train with a MG transmission implemented, as shown in Fig. 1.5, for the same physical motor size. There are several disadvantages of using such a high speed motor which includes: very sensitive to high iron losses, therefore, thinner lamination steel is needed. High speed bearings are needed which are expensive and the bearing losses increase with speed. Another concern of such high speed is the mechanical strength of the rotor due to the high centrifugal forces. Note that a lower speed motor can be used but the volumetric size of the motor will increase with more or less the same factor as with what the speed decreased.

From Fig. 1.4 it is evident that a vehicle with a MG transmission can ascend a very steep road gradient in 1st gear while maintaining a reasonable top speed in 5th gear. This makes the MG transmission favourable for load carrying vehicles with high tractive effort require-

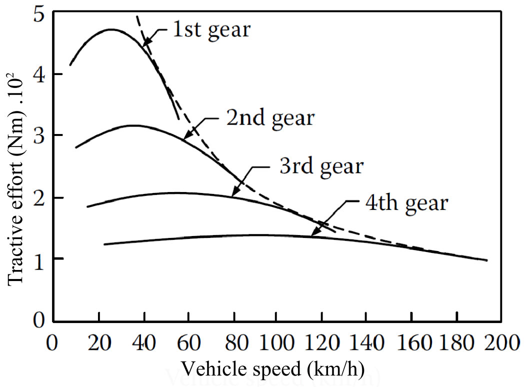

Figure 1.3: Tractive effort of ICE with MG transmission.

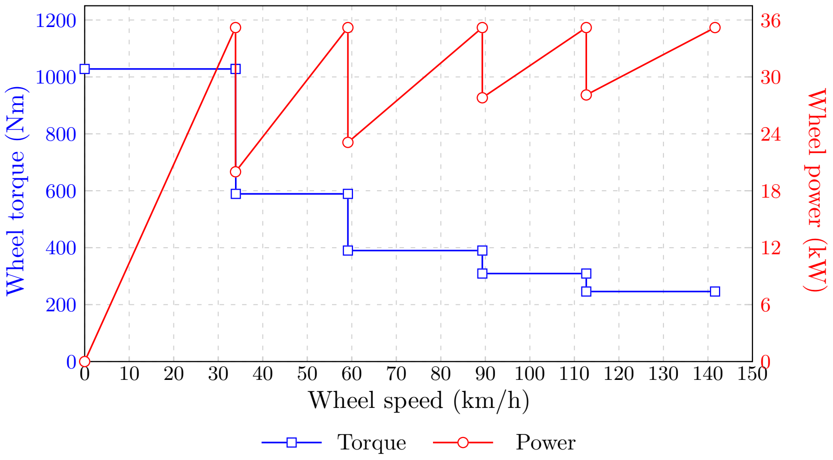

Figure 1.4: Tractive effort of the Opel Corsa 1.4i Lite vehicle with 5-speed MG transmission.

ments for eg. buses, trucks and agriculture vehicles [13, 19]. The fact that MG transmission provides the flexibility to modify the tractive effort profile to match the load requirement is a big advantage over FG EV drives.

The FI-PM machines in this thesis are designed and optimised for the standard MG transmission drive-train of the Opel Corsa 1.4i Lite, therefore, no FW is needed and thus not investigated. However, the FI-PM machine has a good CPSR performance [1], therefore will perform well with a FG drive-train as well. Having a variable gear drive-train however, brings down the size of the machine as less torque is required on the drive side.

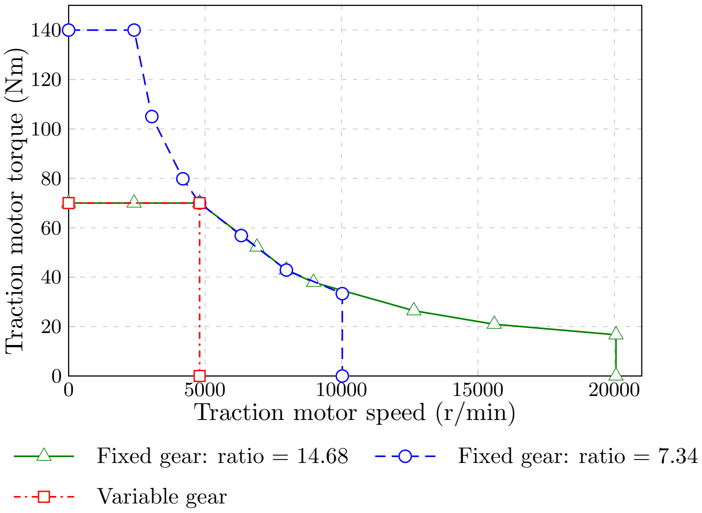

Figure 1.5: Torque-speed graphs for different FG ratios.

1.4 Design specification

The design specifications for the FI-PM traction machine are given in Table 1.1. The specifications are obtained from the vehicle tractive effort of Fig. 1.4. The machines need to fit on the bell-housing of the gearbox and therefore the maximum available outer diameter for the stator is 230 mm. The maximum stack length is 110 mm for the space available in the front-end of the Opel Corsa Lite.

According to the specification of the Opel Corsa, a top wheel speed of 142 km/h need to be achieved in 5^{th} gear. With the wheel outer diameter being 550 mm, the electric traction motor speed needed to achieve the top wheel speed is 4800 r/min. With 1120 Nm needed on the wheels of the EV, the FI-PM machine must produce 70 Nm torque, resulting in rated shaft power of 35 kW.

Note that the air-gap specification is 0.4 mm. The air-gap length is given by the manufacturers as a minimum limit for the physical size of the traction machine.

Table 1.1: Design specifications of electric traction machine

Parameter	Value	Unit
Rated torque	70	Nm
Rated power	35	kW
Rated speed	4800	r/min
Battery pack voltage	350	V DC
Max. stator outer diameter	230	mm
Shaft diameter	43	mm
Max. stack length	110	mm
Min. air-gap length	0.4	mm
Number of poles	4	
Cooling	air	

1.5 Objectives and thesis layout

In this section the objectives of this thesis is given as well as the thesis layout.

Chapter 2:	The objective of this chapter is to derive a mathematical model for the FI-PM machines which is used in the design optimisation of the machines as discussed in Chapter 3. This is achieved by deriving dq equivalent circuits for the FI-PM machine. The calculation of the dq parameters is also explained.
Chapter 3:	The objective of this chapter is to optimise the machines according to the specifications given. The optimisation procedure and method are discussed first and then each machine is optimised for its own objective function. The focus is to reduce expensive PM material. High torque ripple issues is solved by implementing new rotor topologies.
Chapter 4:	The objective of this chapter is to investigate the PM demagnetisation and rotor deformation of the optimum designed machines using the JMAG FE software. PM demagnetisation is investigated at worst case scenario conditions, while the rotor deformation due to centrifugal forces are investigated at the maximum electrical machine speed.
Chapter 5:	The objective of this chapter is to validate the FE calculated results with measured results. The FE results of the optimised machines are given and discussed. Only one of the machines is manufactured and tested to compare with FE calculated results.
Chapter 6:	The objective of this chapter is to determine the saliency performance of the FI-PM machine. The saliency performance determines the sensorless control capability of the machine. The saliency of the optimised machines are compared, and a machine is furthermore optimised to improve saliency performance.
Chapter 7:	This chapter concludes the thesis.

Chapter 2

Mathematical Modelling of the FI-IPM machine

In this chapter the equivalent circuit parameters and equations which describes the FI-PM machine are discussed, which are used in the design optimisation. The power invariant Park's transformation is used to convert the *abc* space phasor model (3-phase AC quantities) with its reference fixed to the stationary stator reference frame, to an equivalent $dq0$ space phasor model (DC quantities) with its reference fixed to the synchronously rotating rotor reference frame. The design optimisation of the FI-PM machines in Chapter 3 are based on steady-state machine operation and therefore the calculations and derivations are based on the latter.

2.1 Equivalent circuit model

The dq equivalent circuits of the FI-PM machine is derived in this section to calculate the dq circuit parameters used in the design optimisation. The model of the *abc* space phasor machine can be simplified using Park's transformation matrix given by

$$\boldsymbol{k}_p = \frac{2}{3}\begin{bmatrix} cos(\theta_e) & cos(\theta_e - 120^\circ) & cos(\theta_e + 120^\circ) \\ -sin(\theta_e) & -sin(\theta_e - 120^\circ) & -sin(\theta_e + 120^\circ) \\ \frac{1}{2} & \frac{1}{2} & \frac{1}{2} \end{bmatrix}, \tag{2.1}$$

where θ_e is the electrical rotor position. The general equation for the 3-phase stator voltage vector, $\boldsymbol{v}_{abc}$, derived from Ohm's and Faraday's laws is given by

$$\boldsymbol{v}_{abc} = r_s \boldsymbol{i}_{abc} + \frac{d\boldsymbol{\lambda}_{abc}}{dt}, \tag{2.2}$$

where $\boldsymbol{v}_{abc}$, $\boldsymbol{i}_{abc}$ and $\boldsymbol{\lambda}_{abc}$ are the stator voltage, current and flux linkage vector matrices respectively and r_s the stator winding phase resistance. Equation (2.2) can be transformed to the $dq0$ reference frame using (2.1) [20] as

$$\begin{aligned} \boldsymbol{v}_{dq0} &= \begin{bmatrix} v_d \\ v_q \\ v_0 \end{bmatrix} = r_s \begin{bmatrix} i_d \\ i_q \\ i_0 \end{bmatrix} + \frac{d}{dt} \begin{bmatrix} \lambda_d \\ \lambda_q \\ \lambda_0 \end{bmatrix} + \omega_e \begin{bmatrix} -\lambda_q \\ \lambda_d \\ 0 \end{bmatrix} && (2.3) \\ &= r_s \boldsymbol{i}_{dqo} + \frac{d\boldsymbol{\lambda}_{dqo}}{dt} + \omega_e \boldsymbol{\lambda}_{dqo}, && (2.4) \end{aligned}$$

where ω_e is the electrical rotor speed.

For the steady-state design optimisation in Chapter 3 the d- and q-axis currents are DC values so that [21]

$$\frac{d\lambda_d}{dt} = \frac{\partial \lambda_d}{\partial i_d}\frac{di_d}{dt} + \frac{\partial \lambda_d}{\partial i_q}\frac{di_q}{dt} = 0 \quad \text{and} \quad \frac{d\lambda_q}{dt} = \frac{\partial \lambda_q}{\partial i_q}\frac{di_q}{dt} + \frac{\partial \lambda_q}{\partial i_d}\frac{di_d}{dt} = 0 \tag{2.5}$$

therefore,

$$\begin{aligned} \boldsymbol{V}_{dq0} &= \begin{bmatrix} V_d \\ V_q \\ V_0 \end{bmatrix} = r_s \begin{bmatrix} I_d \\ I_q \\ I_0 \end{bmatrix} + \omega_e \begin{bmatrix} -\lambda_q \\ \lambda_d \\ 0 \end{bmatrix} && (2.6) \\ &= r_s \boldsymbol{I}_{dqo} + \omega_e \boldsymbol{\lambda}_{dqo}. && (2.7) \end{aligned}$$

Assuming a balanced 3-phase system, the zero sequence component, V_0, becomes zero and the equations reduce to dq models only. The flux linkages λ_d and λ_q includes the end-winding flux linkage λ_e, leakage flux linkage λ_l and the fundamental stator winding air-gap flux linkage λ_g. The d-axis flux linkage also includes the PM flux linkage λ_{PM}, which is situated on the

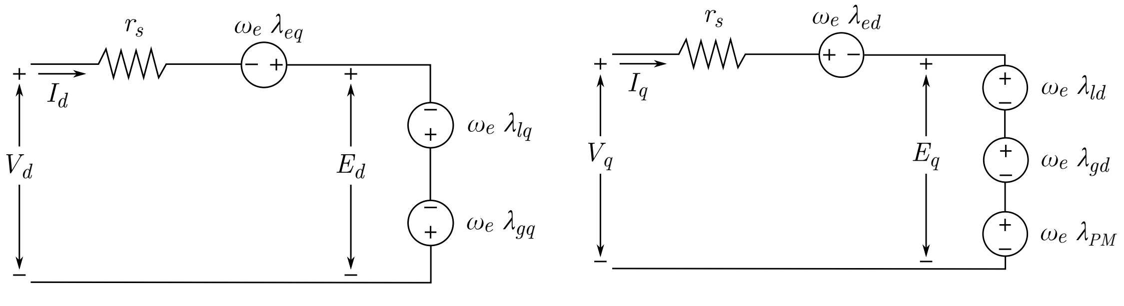

(a) d-axis (b) q-axis

Figure 2.1: Steady-state d- and q-axis equivalent circuits of the FI-PM machine.

d-axis of the rotor. The dq equivalent circuit models of the FI-PM machine are composed from (2.7) as shown in Fig. 2.1.

2.2 Calculation of equivalent dq circuit parameters

In this section the equivalent dq parameters of Fig. 2.1 are calculated which is used in the design optimisation.

2.2.1 Phase resistance

The stator winding phase resistance, r_s, is calculated by

$$r_s = \frac{2N\rho_t(\ell_s + \ell_e)}{n_a \frac{A_{cu}}{z}}, \tag{2.8}$$

where N is the number of turns in series per phase, ℓ_s the active stack length, ℓ_e the end-winding length, n_a the number of parallel circuits of the stator winding, A_{cu} the active copper area per slot and z being the number of turns per slot. The slot fill factor must be taken into account when calculating the active copper area per slot A_{cu} from the slot dimensions. The fill factor is the ratio of the active copper area over the total slot area, thus, taking the stator slot and copper wire insulation into account when filling a slot. In this thesis a fill factor of 0.47 is used. ρ_t is the resistivity of copper at a temperature t_c calculated by

$$\rho_t = \rho_{20}(1 + Y_t(t_c - 20)), \tag{2.9}$$

where $\rho_{20} = 17 \times 10^{-9}\ \Omega m$ and $Y_t = 0.0039\ ^{\circ}C^{-1}$ for copper.

2.2.2 dq currents

The current density value J is a good indicator, for quick reference, of the copper loss and the associated heat developed in the slot [21], thus, a function of the cooling system design of a machine. Depending on the cooling system design, a value for the current density is chosen in the design optimisation. From the current density, the current magnitude I_s can be determined using

$$I_s = \frac{\sqrt{2} J A_{cu} n_a}{z}. \tag{2.10}$$

The current space phasor can be calculated by

$$\begin{aligned} \boldsymbol{I_s} &= I_s \angle \phi = I_d + jI_q \quad \text{with} && (2.11)\\ I_d &= I_s cos(\phi) \quad \text{and} && (2.12)\\ I_q &= I_s sin(\phi), && (2.13) \end{aligned}$$

where ϕ is the current space phasor angle shown in Fig. 2.2. The current space phasor angle ϕ is a variable in the design optimisation since the torque is a function of it [22].

2.2.3 Flux linkage

In this section the air-gap flux linkage is calculated by means of FE software, and an analytical approximation is given for the end-winding leakage flux.

2.2.3.1 Air gap flux linkage

The JMAG FE package is used to calculate the air-gap flux linkage in this section. The flux linkage of a phase winding is calculated by JMAG using a first-order triangular mesh in the FE analysis and solving for the magnetic vector potential A and integrating along the coil paths. With only a section of the machine meshed, the phase flux linkage, excluding the end-winding flux linkage, is calculated by [21]

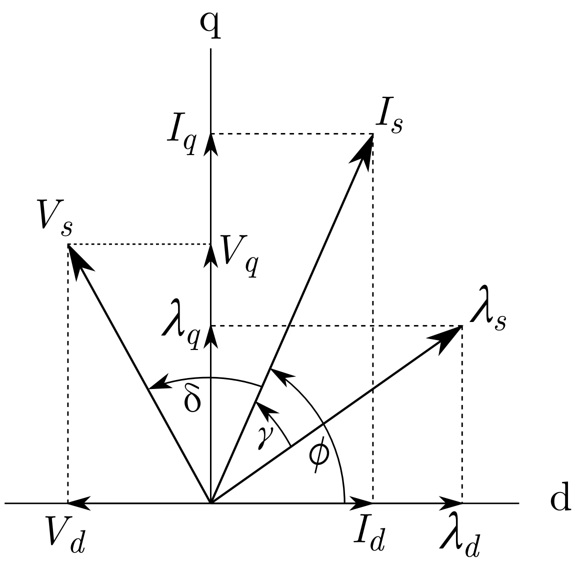

Figure 2.2: Space phasor diagram fixed in the rotating rotor reference frame.

$$\lambda_a = \frac{4pz\ell_s}{n_a A_s} \sum_{j=1}^{y} \left(\frac{\Delta_j \zeta}{3} \sum_{i=1}^{3} A_{ij} \right), \tag{2.14}$$

where A_{ij} is the value of the magnetic vector potential of node $i = 1$, 2 or 3 of the triangular element j. $\zeta = \pm 1$ gives the direction of integration with Δ_j the area of the triangular element j. y is the total number of elements of the meshed coils per phase per pole. A_s is the coil area, ℓ_s the stack length and p the number of pole pairs.

The dq flux linkages can now be calculated from the abc flux linkages using Park's transformation. The d-axis flux linkages includes the stator winding air-gap flux linkage λ_g, leakage flux λ_l, and the PM flux λ_{PM}, while the q-axis flux linkage only includes the stator winding air-gap flux linkage and leakage flux given by

$$\lambda_d = \lambda_{gd} + \lambda_{ld} + \lambda_{PM} \quad \text{and} \tag{2.15}$$

$$\lambda_q = \lambda_{gq} + \lambda_{lq}. \tag{2.16}$$

The flux linkage space phasor λ_s, shown in Fig. 2.2, can now be calculated similar to (2.11) as

$$\boldsymbol{\lambda_s} = \lambda\angle(\phi-\gamma) = \lambda_d + j\lambda_q \quad \text{with} \tag{2.17}$$

$$\lambda_d = \lambda_s cos(\phi-\gamma) \quad \text{and} \tag{2.18}$$

$$\lambda_q = \lambda_s sin(\phi-\gamma). \tag{2.19}$$

2.2.3.2 End-winding leakage flux

An approximate end-winding leakage inductance formula is obtained from the study in [22] as

$$L_e = 4.55 \times 10^{-7} d_{si} W^2, \tag{2.20}$$

where d_{si} is the stator bore inner diameter and W the amount of turns in series per phase. From (2.20) the end-winding leakage flux can be calculated for the d- and q-axis by

$$\lambda_{ed} = L_e I_d \quad \text{and} \tag{2.21}$$

$$\lambda_{eq} = L_q I_q \tag{2.22}$$

respectively.

2.2.4 dq voltages

The voltage space phasor, $\boldsymbol{V_s}$ shown in Fig. 2.2, is also calculated similar to (2.11) as

$$\boldsymbol{V_s} = V_d + jV_q \quad \text{with} \tag{2.23}$$

$$V_d = I_d r_s - \omega(\lambda_{gq} + \lambda_{lq} + \lambda_{eq}) \quad \text{and} \tag{2.24}$$

$$V_q = I_q r_s + \omega(\lambda_{gd} + \lambda_{ld} + \lambda_{ed} + \lambda_{PM}). \tag{2.25}$$

The dq voltages are based on the steady-state equivalent circuit in Fig. 2.1.

2.3 Torque

The JMAG 2D FE software was using a time stepping method and therefore the magnetic fields can be considered as static for each step or rotor position. The instantaneous torque of the FI-PM machine is therefore calculated using the well-known Maxwell's stress Tensor method (MST). The model is stepped through only one torque periodicity, which in this case is $60°e$ for a 4-pole machine, to get accurate torque versus rotor position detail and reduce computation time. The average torque used in the design optimisation is calculated from the instantaneous torque as

$$T_{avg} = \frac{1}{n}\sum_{i=0}^{n} T_{inst}(\theta_i), \tag{2.26}$$

where n is the number of position steps and T_{inst} the instantaneous torque at rotor position θ_i. The instantaneous torque T_{inst} is calculated using the MST method as

$$T_{inst} = \frac{1}{\mu_0}\oint_{\Gamma} rB_tB_n \cdot d\Gamma \times \ell_s, \tag{2.27}$$

where μ_0 is the permeability of free space, r the radius of the contour Γ in the centre of the air-gap. B_n and B_t are the normal and tangential flux densities in the air-gap respectively, calculated from the magnetic vector potentials [24] and ℓ_s is the stack length. The electromagnetic torque can also be expressed as a function of the current space phasor angle as

$$T_{em} = \frac{3}{4}p(L_d - Lq)i_s^2 sin(2\phi) + \frac{3}{2}p\lambda_{PM}\, i_s sin(\phi), \tag{2.28}$$

where the term $L_d - L_q$ is the saliency and L_d and L_q are the d- and q-axis inductances due to the stator air-gap flux linkages respectively. From the instantaneous and average torques the peak-to-peak torque ripple used in the design optimisation is calculated by

$$T_{rip} = \left(\frac{T_{max} - T_{min}}{T_{avg}}\right) 100\%. \tag{2.29}$$

2.4 Efficiency

In the design optimisation of Chapter 3 only the copper losses are considered, as the major part of the losses consist of it [25]. The efficiency, which also includes the iron and rotational losses, is excluded in the design optimisation and evaluated afterwards for the final designed machines. Thus, the iron losses are not included in the equivalent circuits of Fig. 2.1. The efficiency of the optimum designed machines is calculated afterwards by

$$\eta = \frac{P_{out}}{P_{out} + P_{cu} + P_{fe} + P_{rot}}, \tag{2.30}$$

where P_{out} is the output power on the shaft and P_{cu} the copper losses calculated from (2.11) and (2.8) as

$$P_{cu} = \frac{3}{2} I_s^2 r_s. \tag{2.31}$$

P_{fe} is the iron losses, consisting of hysteresis and eddy-current losses, in the rotor and stator laminations. The lamination material used are 20HTH1200 and 50A230 for the stator and rotor respectively. Note that the stator lamination is thinner than the rotor's to reduce the high eddy-current losses in the stator at high stator frequencies. The iron losses are calculated using the loss calculation tool integrated in the JMAG FE software. The hysteresis loss is given by

$$P_h = \sum_{e=1}^{E} \left\{ \sum_{k=1}^{N} \alpha_b \left(|B_k| \right) \cdot f_k \right\} V_e, \tag{2.32}$$

where α is the coefficient of the magnetic flux density $|B_k|$ for harmonic order k determined by the frequency separation method, f_k is the frequency for harmonic order k, V_e is the volume of each element, N is the maximum frequency order and E is the number of elements. The eddy-current losses are given by

$$P_e = \sum_{e=1}^{E} \left\{ \sum_{k=1}^{N} \alpha_b \left(|B_k|, f_k \right) \cdot f_k^2 \right\} V_e, \tag{2.33}$$

The total iron loss obtained from (2.32) and (2.33) is multiplied by a factor of 20%, which is added to account for excess loss [21]. Note that the PM loss consisting of hysteresis loss is not included in the calculation due to unavailable loss curves from the FE software material data base for the PM used.

The rotational losses, P_{rot}, consisting of the windage and friction loss are approximated by the following formula's [26]:

$$P_{fric} = k_{fb} G_r n \times 10^{-3} \quad \text{and} \tag{2.34}$$

$$P_{wind} = 2 d_r^3 \ell_s n^3 \times 10^{-3}, \tag{2.35}$$

where k_{fb} is a constant, G_r the mass of the rotor, n the rotational speed, d_r the rotor outer diameter and ℓ_s the stack length.

Chapter 3

FE Design Optimisation

The design optimisation of the FI-PM machines are done by means of optimisation algorithms of the VisualDoc software [27] together with Python scripts and JMAG FE simulation software. The optimisation is an iterative process where optimisation algorithms repeatedly call the FE software, using Python scripts, to calculate the objective function and other performance parameters. The optimisation algorithms used are gradient-based algorithms for constrained problems which make use of one-dimensional search methods, also known as line search methods.

3.1 Optimisation theory

3.1.1 Constrained optimisation algorithms

There are two ways to approach constrained optimisation problems. The first approach is called the Sequential Unconstrained Minimisation Technique (SUMT) and the second is the direct method. The SUMT approach solves the constrained optimisation problem by first converting it to an equivalent unconstrained problem. This equivalent unconstrained problem is then solved using unconstrained algorithms. The SUMT methods have become less popular as the direct or constrained methods became more mature and efficient, although the SUMT method is still a popular choice for problems with a very large amount of design variables [28]. The direct methods on the other hand directly solves the non-linear constrained optimisation problem. Today, the gradient-based technique of choice for constrained optimisation problems with few design variables, as in this thesis, are direct methods [28].

Gradient-based optimisation algorithms are mostly local type of algorithms. This means that the optimisation may reach a local minimum (maximum) instead of the global minimum (maximum), shown in Fig. 3.1 for a simple two variable optimisation problem.

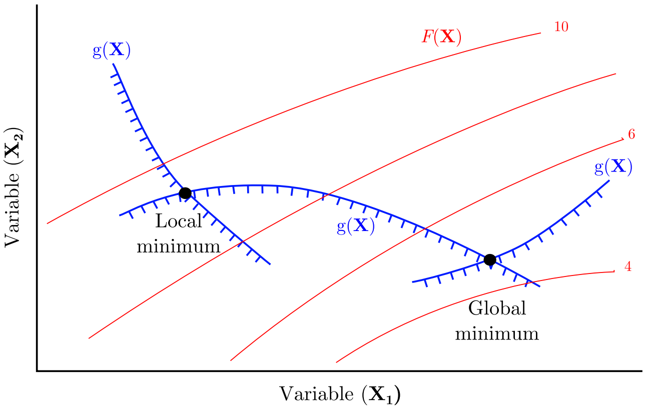

Figure 3.1: Local and global minimums.

The author verified the final designs to ensure that no local minimums (maximums) were obtained by running several optimisations with different initial design variables. The criteria is to obtain the same (or within a very fine margin) value for the objective function with different initial design variables in order to avoid local minimums (maximums).

The gradient-based constrained algorithms commonly encountered in engineering today and available in the VisualDoc software are:

- Modified Method of Feasible Direction (MMFD)
- Sequential Quadratic Programming (SQP)
- Sequential Linear Programming (SLP)

The method used in this thesis is the MMFD and will be discussed in the next section.

3.1.2 Optimisation process

The optimisation algorithm finds a multi-dimensional vector [**X**] that minimises or maximises the objective function (performance parameter) F of the machine subject to inequality and/or equality constraints. The multi-dimensional vector [**X**] includes amongst other things the physical dimensions of the machine, i.e the machine design variables. For each iteration r of the optimisation process, a direction of search is determined where $[\mathbf{X}]$ is changed within a multi-dimensional search space to minimise or maximise the objective function. The multi-dimensional space or searchable design space, as referred to by [28], is defined by the upper and lower bounds set for each of the design variables in $[\mathbf{X}]$ also known as side constraints. For each iteration r, several sub-iterations take place which search in the determined direction which is known as the line search. The line search continues until no progress can be made anymore which might include reaching a constraint. A new search direction is then determined from the gradient information for the next iteration r and the line search process is repeated. The process above can mathematically be explained as follow:

$$\textit{minimize}\, F(\mathbf{X}) \qquad \text{subject to} \tag{3.1}$$

$$\mathbf{g}(X) <,> \mathbb{R} \tag{3.2}$$

$$\mathbf{h}(X) = \mathbb{R} \tag{3.3}$$

$$\mathbf{X}_L \leq \mathbf{X} \leq \mathbf{X}_U \tag{3.4}$$

where $\mathbf{g}(X)$ is the vector containing the inequality constraints, $\mathbf{h}(X)$ the vector containing the equality constraints and $\mathbf{X}_L$, $\mathbf{X}_U$ are the lower and upper side constraint vectors respectively which defines the searchable design space. The direction of search for the first iteration is determined by the gradient of the objective function to be minimised given in (3.5), assuming that the starting point is within the constraints.

$$\mathbf{S}_1 = -\nabla F(\mathbf{X}_0) \tag{3.5}$$

In (3.5) $\mathbf{S}_1$ is the vector search direction of the first iteration and $\mathbf{X}_0$ the vector containing the initial design variables. The gradient of the objective function is

$$\nabla F = \begin{bmatrix} \frac{\partial}{\partial X_1} F(\mathbf{X}) \\ \frac{\partial}{\partial X_2} F(\mathbf{X}) \\ \dots \\ \frac{\partial}{\partial X_n} F(\mathbf{X}) \end{bmatrix}, \tag{3.6}$$

which ensures that the search direction is directed towards the optimum where X_1, $X_2 \dots X_n$ are the individual design variables. All the design variables in the optimisation are scaled to a value of one. The optimisation now searches in this direction until it reaches a constraint or a minimum (maximum). Every sub-iteration is a step in this direction. This procedure is called the line search and the new location (reaching a constraint or minimum/maximum) can be updated by the following expression

$$\mathbf{X}_q = \mathbf{X}_{q-1} + \alpha \mathbf{S}_q, \tag{3.7}$$

where q denotes the iteration number, $\mathbf{S}$ the vector search direction and α, the step size.

Unlike the SQP and SLP methods, the MMFD algorithm calculates a search direction that follows the constraint bounds rather than moving inside the searchable design space towards the optimum. For the next search direction $\mathbf{S}_2$, a usable and feasible direction must be calculated. A *usable* direction ensures that the search direction is towards the optimum that will improve the design, which can mathematically be defined by [27]

$$\nabla F(\mathbf{X})^T \cdot \mathbf{S} \leq 0, \tag{3.8}$$

while a *feasible* direction is one that ensure that the search direction is tangent to or away from the constraint bounds mathematically defined by [27]

$$\nabla g_j(\mathbf{X})^T \cdot \mathbf{S} \leq 0, \tag{3.9}$$

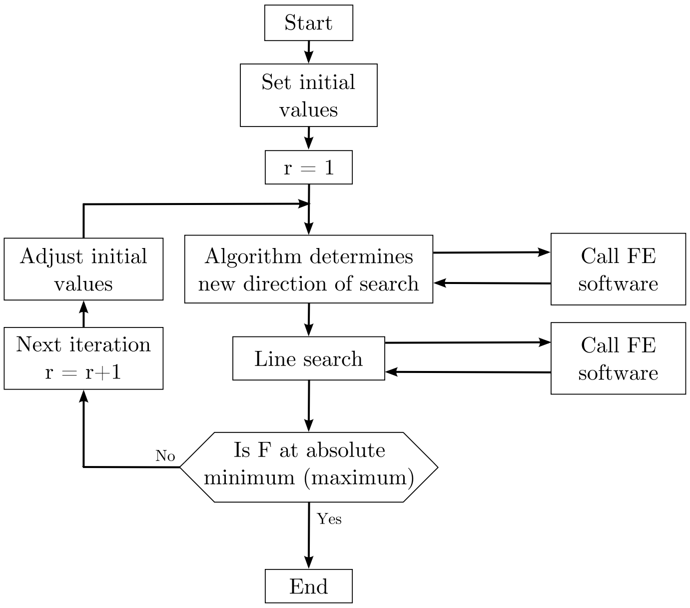

Figure 3.2: Optimisation process flowchart.

where j denotes the constraints that are close to the updated location with some numerical tolerance. The usability and feasibility requirements is then combined so that the search direction is one that will make the greatest possible improvement in F while moving inside the constraints [27].

This iterative process continues until the objective function reaches a maximum (minimum) while the inequality and/or equality constraints are met. The optimisation process may be explained by the flowchart shown in Fig. 3.2.

3.2 FI-PM machine optimisation

Two FI-PM machines are designed. The first machine design is a preliminary design with a basic rotor structure and few design variables, while the second machine design has a more complex rotor structure which contain internal flux barriers. With internal flux barriers the reluctance torque is increased, therefore, the stack length reduces, thus, the PM volume.

The performance design specifications are according to the tractive effort and power specification for each gear of the ICE of the Opel Corsa 1.4i with 5-speed MG transmission. The tractive effort and power specifications of the vehicle are shown in Fig. 1.4. From the vehicle specifications the electric machine specifications are determined as tabulated in Table 1.1. The machines are optimised for steady-state conditions at rated speed and torque of 4800 r/min and 70 Nm respectively.

3.2.1 Pre-optimisation discussion

The stator of the first machine, called Basic Rotor FI-PM (BR-FI-PM) machine, is not optimised as a stator of a previously designed and manufactured RSM for the Corsa (for the same specifications) is used for testing purposes. Hence, the active stack length and winding layout of the first machine design are fixed. All the machines designed are 4 pole machines with 36-slot stators. The BR-FI-PM machine has a stator with a 7/9 chorded winding. Torque ripple can be reduced by choosing the right chording ratio without affecting the average torque too much. To determine which chording ratio is best for torque ripple, the winding factors for the different chord ratios must be determined. The winding factor is calculated by

$$k_{w\nu} = k_{d\nu} k_{p\nu}, \tag{3.10}$$

where $k_{d\nu}$ and $k_{p\nu}$ are the distribution and pitch factors respectively at harmonic order ν, calculated by

$$k_{d\nu} = \frac{sin(\nu \frac{q\alpha_u}{2})}{q\, sin(\nu \frac{\alpha_u}{2})} \qquad (3.11) \qquad \text{and} \qquad k_{p\nu} = sin(\nu \frac{w\pi}{\tau_p 2}), \qquad (3.12)$$

where q is the amount of slots per pole phase group, α_u the slot pitch, w the coil-span pitch and τ_p the pole pitch. The calculated results for the winding factor are given in Table 3.1 for the different chording ratios.

The fundamental winding factor, $\nu = 1$, gives a indication by how much the average torque will reduce from the full pitch winding (9/9 chord), while the 5^{th} and 7^{th} harmonic orders of the winding factor give an indication how the torque ripple is affected [29]. From Table 3.1 it is evident that the average torque will reduce by 1.52% from a full pitch winding to a 8/9 chorded winding while a decrease of 6.03% is is evident for a 7/9 chorded winding.

Table 3.1: Winding factors calculated for different chording ratios.

Chord ratio	$\nu = 1$	$\nu = 5$	$\nu = 7$
9/9	0.9598	0.2176	0.1774
8/9	0.9452	0.1398	0.0607
7/9	0.9019	-0.0378	-0.1359

It must be remembered that the winding factors only gives an indication by how much the parameters are affected. The combination of the 5^{th} and 7^{th} harmonic reduces by almost the same amount for a 8/9 and 7/9 chording from full pitch. The torque ripple hence for the two chording ratios will therefore reduce by almost the same amount. This is also observed by [29]. From the fundamental winding factors it is evident that a 8/9 chord ratio is a better option since there is only a 1.52% decrease in average torque. From this, the second machine, called the Flux Barrier Rotor FI-PM (FBR-FI-PM) machine, has a 36-slot stator with an 8/9 chorded winding.

The materials used for the stator lamination, rotor lamination and PM's are 20HTH1200, 50A230 and S45SH respectively. Note that the stator lamination is thinner than the rotor lamination to reduce eddy-current losses in the stator at high stator frequencies.

3.2.2 Design optimisation of Basic Rotor FI-PM machine

The BR-FI-PM machine has a very simple rotor geometry, therefore it is easy to optimise and manufacture. The rotor structure have big cut-outs in the iron across the q-axis flux paths as shown in Fig. 3.3 With the cut-outs, the effective air-gap along the q-axis increases resulting in the q-axis inductance L_q to decrease. In this way $L_d > L_q$. The cut-out shape is obtained by using a parabola in the design optimisation which is much more flexible than using a half circle. Due to the parabola the cut-out shape can be deep and narrow to obtain a large inductance difference without sacrificing active rotor surface. The rotor structure contains only three design variables due to its simplicity as shown in Fig. 3.3. The simple rotor structure has the advantage of eliminating mechanical issues such as mechanical stress and deformation of the rotor due to centrifugal forces, which are issues in the design of [30] and [31]. The simple rotor structure is also less expensive to manufacture.

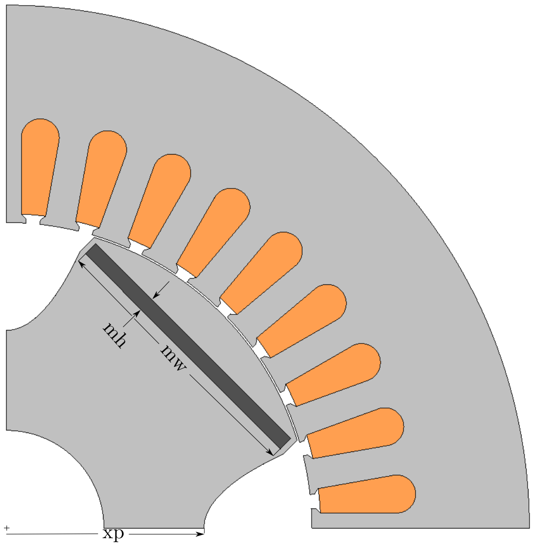

Figure 3.3: Quarter cross-section of the BR-FI-PM machine showing the rotor design variables. The stator variables are fixed and are not shown.

The objective function in the optimisation is to minimise the PM volume subject to a torque constraint since it contains expensive rare earth materials, therefore, reducing cost. By reducing the PM volume the PM thickness will reduce, which will cause the d-axis inductance L_d to increase due to the located PM on the d-axis, and is favourable for FI-PM machines. The PM thickness can be reduced with minimised risk of PM demagnetisation. The PM demagnetisation risk is minimised due to the FI operation which is opposite of FW which try to demagnetise the PM's due to large negative d-axis currents [30]. However, careful attention must be paid to temperature rise and the armature reaction effect which tend to demagnetise the PM if it is too thin. The PM width is fixed within a distance of 1.1 mm to the pole width, therefore, as the PM width change in the design optimisation, the pole width changes accordingly.

From the rated current of the given stator, the current density J in the optimisation is calculated to be 8.49 A.mm^{-2}. From the the dq currents and current density the other parameters of the equivalent circuits in Chapter 2, used in the design optimisation, are calculated. The objective function to be minimised is expressed as

$$F(\mathbf{X}) = V_{PM}(\mathbf{X}) \tag{3.13}$$

subject to the constraint of

$$\mathbf{g} = \begin{bmatrix} T_{avg} \end{bmatrix} > \begin{bmatrix} 70.0 \end{bmatrix} \tag{3.14}$$

and constants as

$$\mathbf{u} = \begin{bmatrix} ro_{od} \\ ro_{id} \\ \ell_s \end{bmatrix} = \begin{bmatrix} 133.6 \\ 43.0 \\ 110.0 \end{bmatrix}, \tag{3.15}$$

where the matrix vector $\mathbf{X}$ includes the design variables as

$$\mathbf{X}^{\mathrm{T}} = \begin{bmatrix} \phi & x_p & m_w & m_h \end{bmatrix}. \tag{3.16}$$

Since the torque is a function of the current space phasor angle ϕ as given in (2.28), it is a variable in the design optimisation as given in (3.16), to ensure the optimum angle for maximum torque while using minimum PM volume. The optimum PM height m_h found from the optimisation was 2.0 mm, but, due to the fragility of the PM and manufacturing constraints the height was specified by the manufacturers not to be smaller than 3 mm and was changed in the optimisation accordingly. The optimum values for the design variables obtained from the optimisation are given in Table 3.2. From the PM height m_h, PM width m_w and stack length ℓ_s the PM volume of the machine is determined to be 80.05 cm^3. The performance results of the optimised machine are discussed in the next chapter.

Table 3.2: Optimum design variables obtained from the optimisation for the BR-FI-PM machine.

Variables	ϕ	x_p	m_w	m_h
Values	71.0	43.457	30.32	3.0

3.2.3 FI-PM machine with internal flux barriers optimisation

The rotor structure of the FBR-FI-PM machine to be optimised consist of flux barriers across the q-axis flux paths in order to reduce the q-axis inductance L_q and cause $L_d > L_q$. The flux barriers improves the saliency of the machine, therefore, the reluctance torque will increase and less PM torque is needed to meet the torque requirements, thus, less PM material is needed. The saliency improvement is also advantageous for sensorless control which is discussed in Chapter 6.

The FBR-FI-PM machine has a lot more design variables than the BR-FI-PM machine due to its complex rotor structure and the stator which is also optimised. The stator has three design variables while the rotor has fourteen design variables shown in Fig. 3.4a.

In the optimisation of the BR-FI-PM machine it was observed that the PM height m_h decreased to a value below the allowed minimum. Therefore the PM height is fixed in this optimisation at 3 mm due to the fact that even more torque will be produced because of the high q-axis reluctance paths the flux barriers are creating. The PM width m_w is fixed within a distance of 1.1 mm to the tip of the outer flux barrier, therefore, as the pitch of the outer

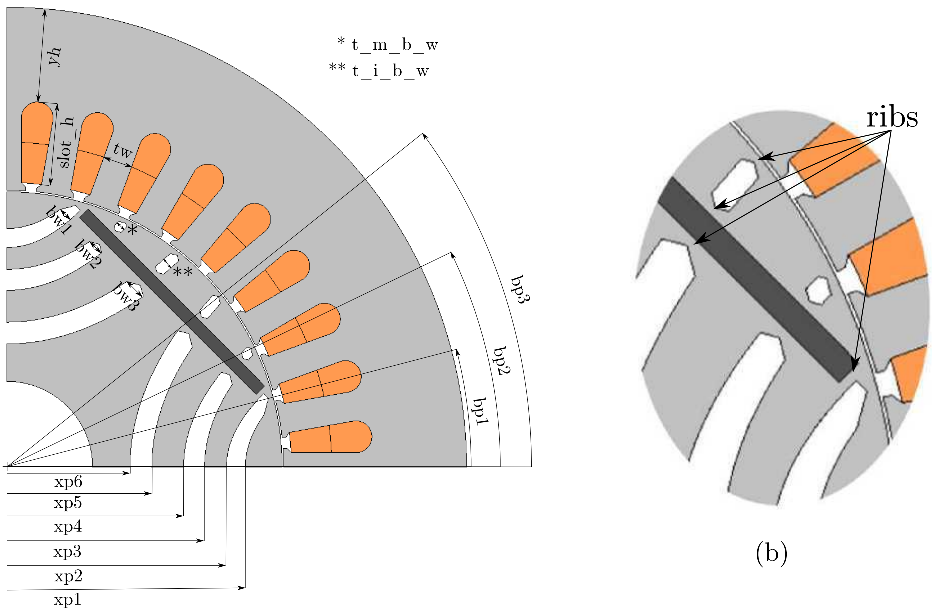

(a)

(b)

Figure 3.4: (a) Quarter cross-section showing the design variables of the FBR-FI-PM machine. (b) An enlarged section of the quarter cross-section showing the iron ribs.

barrier changes in the design optimisation, the PM width changes accordingly.

The pitch of the flux barriers is an important design parameter as the torque ripple is greatly influenced by the position of the tips of the flux barriers [33]. The iron ribs in the rotor has a thickness of 1.1 mm to prevent mechanical failure at maximum speed. The ribs are indicated in Fig. 3.4b.

The objective function is to minimise the $\frac{P_{cu}}{T_{avg}}$. Since the major part of the losses in this machine comprises of copper loss [25], optimising $\frac{P_{cu}}{T_{avg}}$ is close to optimising the efficiency of the machine [22]. The current density J in the optimisation is 8.5 A.mm^{-2}. From the current density the dq currents and other parameters of the equivalent circuits in Chapter 2, used in the design optimisation, are calculated.

The objective function to be minimised is expressed as

$$F(\mathbf{X}) = \frac{P_{cu}}{T_{avg}}(\mathbf{X}) \tag{3.17}$$

subject to the constraints of

$$\mathbf{g} = \begin{bmatrix} 70.0 \\ 0.0 \end{bmatrix} < \begin{bmatrix} T_{avg} \\ T_{rip} \end{bmatrix} < \begin{bmatrix} 74.0 \\ 20.0 \end{bmatrix} \tag{3.18}$$

and constants as

$$\mathbf{u} = \begin{bmatrix} st_{od} \\ ro_{id} \\ \ell_g \end{bmatrix} = \begin{bmatrix} 230.0 \\ 43.0 \\ 0.4 \end{bmatrix}, \tag{3.19}$$

where the matrix vector $\mathbf{X}$ includes the design variables as

$$\mathbf{X}^{\mathrm{T}} = \begin{bmatrix} \phi & \ell_s & y_h & slot_h & t_w & t\_i\_b_w & t\_m\_b_w & x_{p1} & x_{p2} & x_{p3}... \\ ... & x_{p4} & x_{p5} & x_{p6} & bp_1 & bp_2 & bp_3 & bw_1 & bw_2 & bw_3 \end{bmatrix}. \tag{3.20}$$

Table 3.3: $\frac{P_{cu}}{T}$ as a function of ℓ_s.

ℓ_s	T_{avg}	P_{cu}	$\frac{P_{cu}}{T_{avg}}$
90.0	71.05	1.1257	15.85
100.0	78.94	1.1591	14.68
110.0	86.83	1.1925	13.73

The current space phasor angle ϕ is again a variable in the design optimisation to ensure maximum torque, thus, minimum $\frac{P_{cu}}{T_{avg}}$. Also the stack length ℓ_s in this case is a variable to ensure the minimum length for the FBR-FI-PM machine. Note that torque constraint in (3.18) has a upper and lower bound. The lower bound is implemented so that the machine reaches the torque specification, while the upper bound is to prevent ℓ_s from increasing. If there is no upper bound the stack length keeps on increasing due to the gain in torque. The gain in torque is, however, greater than the gain in copper loss for an increase in ℓ_s, thus, decreasing $\frac{P_{cu}}{T_{avg}}$. This is shown for a FBR-FI-PM machine with different stack length values in Table 3.3 for example. If no upper bound is implemented the torque will be far over specification due to the long stack length. The shortest possible stack length is desired as less material is needed for manufacturing in this case.

The optimum values for the design variables are given in Table 3.4. Note the 18.27% decrease in ℓ_s from the BR-FI-PM machine. The decrease in ℓ_s is due to the flux barriers in the rotor which generates more reluctance torque than the BR-FI-PM machine. The PM volume decreased by 15.74% to 67.45 cm^3 from what is used in the BR-FI-PM machine.

The FBR-FI-PM machine produces a relatively high torque ripple of 11%, therefore, another optimisation is executed with the torque ripple as the objective function in order to try to reduce it to a lower value without the need for skewing the rotor. The only constraint is the torque which need to be >70 Nm. The design variables are the same as in (3.20). The outcome of the optimisation showed that only the three barrier pitches changed slightly, as given in Table 3.5, reducing the torque ripple by only 9.1%. This shows that the barrier pitches were at the optimum for minimum torque ripple in the optimisation of (3.17) already. An interesting observation is that the barrier pitches correspond more or less to the optimum

Table 3.4: Optimum design variables obtained from the optimisation for the FBR-FI-PM machine.

Variables	Values
δ	84.24
ℓ_s	89.9
y_h	23.35
$slot_h$	22.38
t_w	7.34
$t\_i\_b_w$	2.78
$t\_m\_b_w$	2.39
x_{p1}	59.68

Variables	Values
x_{p2}	54.94
x_{p3}	49.47
x_{p4}	44.22
x_{p5}	36.28
x_{p6}	30.83
bp_1	15.29
bp_2	25.98
bp_3	38.89

Variables	Values
bw_1	3.63
bw_2	4.1
bw_3	5.53

Table 3.5: Optimum barrier pitches obtained from the optimisation for the FBR-FI-PM machine optimised for minimum torque ripple.

Variables	bp_1	bp_2	bp_3
Values	15.15	26.09	38.1

barrier pitches proposed by [32] for minimum torque ripple. The performance results of the optimised machine are discussed in the next chapter.

3.2.4 Asymmetric rotor configuration

The BR-FI-PM and FBR-FI-PM machines exhibit a high torque ripple which can be reduced by skewing the rotor by means of a number of stacks. Due to the PMs it is difficult to skew the machine in the manufacturing process, therefore, a relatively new topology is implemented where the adjacent poles of the machine, or the flux barriers in the adjacent poles, are asymmetric. This topology was first introduced in 2004 by [33]. Several other authors also investigated asymmetric flux barrier arrangements which include [34–36]. One drawback of this topology is that two poles of the machine need to be modelled in the FE software due to the asymmetry in order for the boundary conditions to match. This increases simulation time which is unwanted for FE design optimisation.

3.2.4.1 Asymmetric BR-FI-PM machine

The rotor structure of the optimised BR-FI-PM motor causes a high torque ripple of 39% (performance results are shown in the next chapter). An optimisation with asymmetric poles was conducted where the objective function was to minimise the torque ripple with only the magnet/pole widths as variables shown in Fig. 3.5. The objective function can be expressed as

$$F(\mathbf{X}) = T_{rip}(\mathbf{X}) \tag{3.21}$$

subject to the constraint of

$$\mathbf{g} = \begin{bmatrix} T_{avg} \end{bmatrix} > \begin{bmatrix} 70.0 \end{bmatrix}, \tag{3.22}$$

where the matrix vector $\mathbf{X}$ includes the optimisation variables as

$$\mathbf{X}^{\mathrm{T}} = \begin{bmatrix} mw_1 & mw_2 \end{bmatrix}. \tag{3.23}$$

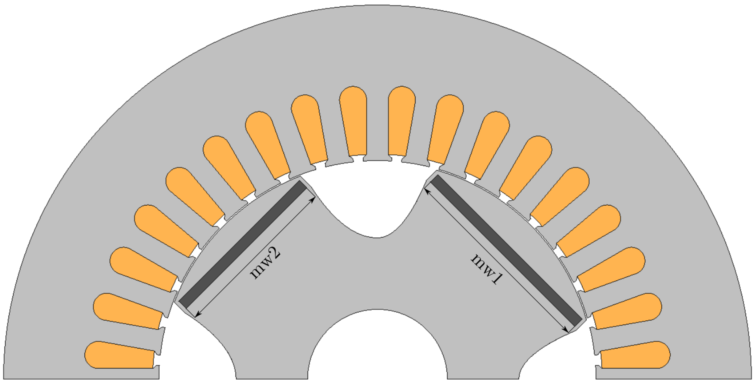

Figure 3.5: Half cross-section showing the design variables of the asymetric BR-FI-PM machine.

Table 3.6: Optimum PM widths found from the optimisation for the asymmetric BR-FI-PM machine.

Variables	mw_1	mw_2
Values	62.78	52.5

All the other design variables in (3.16) were constants in this case.

The optimum values found from the optimisation for the design variables are given in Table 3.6. Note the asymmetry in the pole widths as shown in Fig. 3.5, which causes a decrease of 83.1% in the torque ripple to a value 6.6%.

3.2.4.2 Asymmetric FBR-FI-PM machine

Although the FBR-FI-PM machine's torque ripple is much lower than the BR-FI-PM machine, it is still fairly high and a asymmetric flux barrier configuration was optimised where the flux barriers of the adjacent poles are asymmetric. The objective function and inequality constraint is the same as for the asymmetric BR-FI-PM. The only design variables to be optimised in this case are the barrier pitches as shown in Fig. 3.6. All other design variables in (3.20) are constants. The vector matrix containing the design variables is

$$\mathbf{X}^{\mathrm{T}} = \begin{bmatrix} bp_1 & bp_2 & bp_3 & bp_4 & bp_5 & bp_6 \end{bmatrix}. \tag{3.24}$$

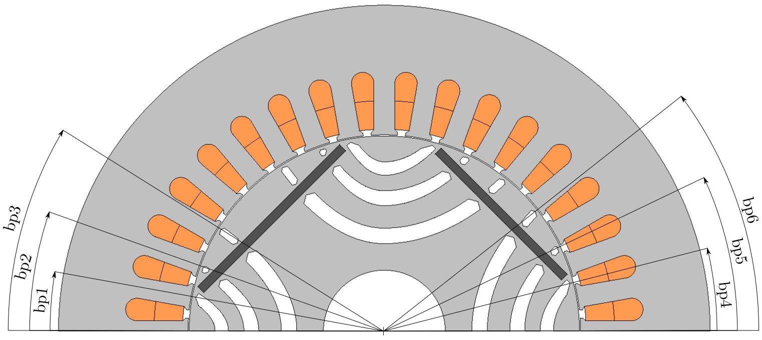

Figure 3.6: Half cross-section showing the design variables of the asymetric FBR-FI-PM machine.

Table 3.7: Optimum flux barrier pitches found from the optimisation for the asymmetric FBR-FI-PM machine.

Variables	Values
bp_1	10.01
bp_2	18.88
bp_3	31.24

Variables	Values
bp_4	14.05
bp_5	25.24
bp_6	38.01

The optimum values found from the optimisation for the design variables are given in Table 3.7. Note the asymmetry in the adjacent flux barrier pitches. The asymmetry caused the torque ripple to decrease with 37.3% to a value of 6.9%.

3.3 Summary

Two FI-PM machines, the BR-FI-PM and FBR-FI-PM machine, were optimised using a gradient-based optimisation algorithm. The BR-FI-PM machine has a very simple rotor geometry, therefore, easy to optimise and to manufacture. The objective was to minimise PM volume since it is expensive and good performance results were obtained. The optimisation reduced the PM height beyond manufacturing capabilities and the height was increased to a specified minimum. The FBR-FI-PM machine produced more reluctance torque due to the increased saliency, therefore, less PM torque is needed to meet the specification and thus less PM material. The PM height was kept fixed at a specified minimum and the objective was to minimise the $\frac{P_{cu}}{T_{avg}}$. Good performance results were obtained. The active stack length of this machine is reduced and therefore also expensive amount of PM material. Both machines exhibit a high torque ripple and a new topology was implemented where adjacent rotor poles/barriers are asymmetric to reduce torque ripple. The new topology implemented was successful in reducing torque ripple.

Chapter 4

PM demagnetisation and rotor deformation

When designing PM machines careful attention must be paid to rotor deformation and especially PM demagnetisation. If the machine fails in one of these two areas the PM thickness and/or iron ribs/bridges must be revised and the machine need to be re-optimised. In this chapter the PM demagnetisation and rotor deformation of the optimum designed machines are investigated using the JMAG FE software.

4.1 PM demagnetisation

All PM's are vulnerable to demagnetisation caused by temperature rise due to losses, high negative d-axis current and armature reaction effect. Although high negative d-axis current is not present due to the FI operation, careful attention must still be paid to demagnetisation due to armature reaction.

The armature reaction effect is explained in Fig. 4.1, which shows the radial flux density over a quarter of the machine for an instance in time and space. It can be seen that negative flux is present over some part of the PM as indicated by the red rectangle, which introduce a risk of demagnetisation if the PM is too thin.

The degree of demagnetisation is calculated by the FE program and is given by

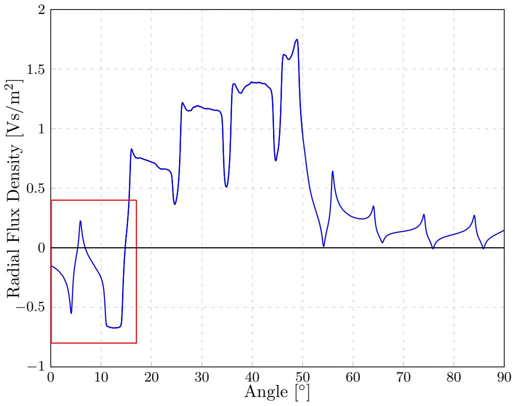

Figure 4.1: armature reaction effect.

$$Demagnetisation\ ratio = \left(1 - \left(\frac{B_1}{B_2}\right)\right) 100, \tag{4.1}$$

where B_1 is the magnitude of the residual flux density of a specified rotor position and B_2 the magnitude of the residual flux density of the current rotor position. The PMs used in the FI-PM machines are Hitachi Metals NMX-S45SH PM material from the JMAG material library. PM demagnetisation risk studies are conducted under worst case scenario conditions for the BR-FI-PM and FBR-FI-PM machines. The worst case scenario conditions are given in Table 4.1 for the two machines.

Figures 4.2a and 4.2b shows the results of the PM demagnetisation studies conducted on the BR-FI-PM and FBR-FI-PM machines respectively. From the figures it is evident that no signs of demagnetisation is visible on the PM surface of the respective machines.

With the temperature constant at 120 $°C$, the current magnitude is increased to determine at which magnitude the PMs starts to show signs of demagnetisation. It was found that the

Table 4.1: Conditions

Parameter	BR-FI-PM	FBR-FI-PM
I_s	320 A_{peak} $\angle 71°$	320 A_{peak} $\angle 84.24°$
PM Temperature	120 $°C$	120 $°C$

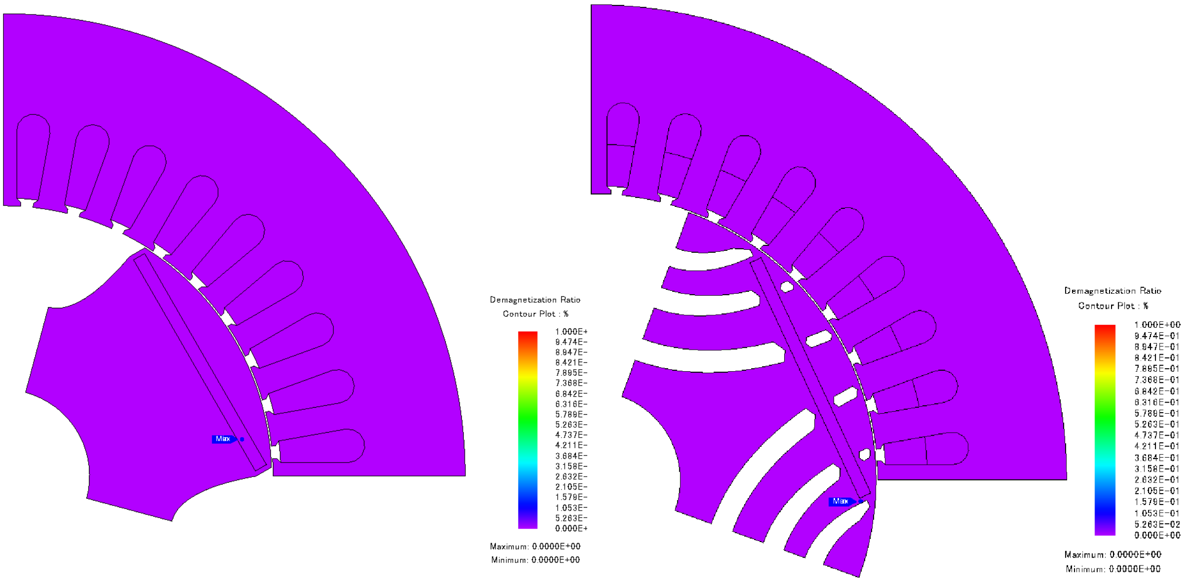

(a) BR-FI-PM machine

(b) FBR-FI-PM machine

Figure 4.2: Quarter cross-sections showing the demagnetisation ratio for (a) the BR-FI-PM machine and (b) the FBR-FI-PM machine for the conditions in Table 4.1.

PM of the BR-FI-PM machine only start to demagnetise at a current magnitude of 340 A shown by the cut-out section of the machine in Fig. 4.3a.

However, the PM of the FBR-FI-PM machine only start to show signs of demagnetisation

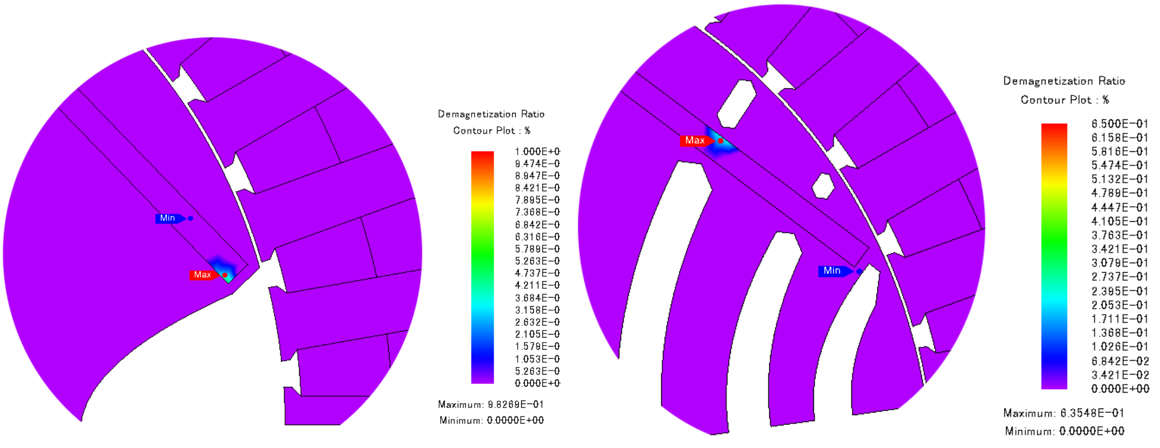

(a) BR-FI-PM machine

(b) FBR-FI-PM machine

Figure 4.3: Cut-out sections showing signs of demagnetisation on the surface of the PMs for (a) the BR-FI-PM machine and (b) the FBR-FI-PM machine.

on the PM surface at a current magnitude of 390 A shown by the cut-out section of the machine in Fig. 4.3b.

The PM demagnetisation of the asymmetric BR-FI-PM and FBR-FI-PM machines will be more or less the same as the symmetric machines and is hence not studied.

4.2 Rotor deformation

Machines rotating at high speeds experience centrifugal forces which introduce a risk of rotor deformation. Deformation of the rotor structure of the FI-PM machines are prevented by giving the iron ribs/webs a sufficient thickness. However, the ribs/webs must not be too thick as leakage flux will increase, thereby reducing torque. A centrifugal force study is done on the FI-PM machines to see whether rotor deformation occurs.

The BR-FI-PM machine shows a radial displacement of 16 μm at a speed of 4800 r/min. Since the air-gap is 0.4 mm the displacement is deemed acceptable. The deformation is shown in Fig. 4.4a, and is not even visible. The red lines show the original shape of the rotor. In Figure 4.4b the deformation is shown with the displacement scaled by one hundred to show how the rotor deforms.

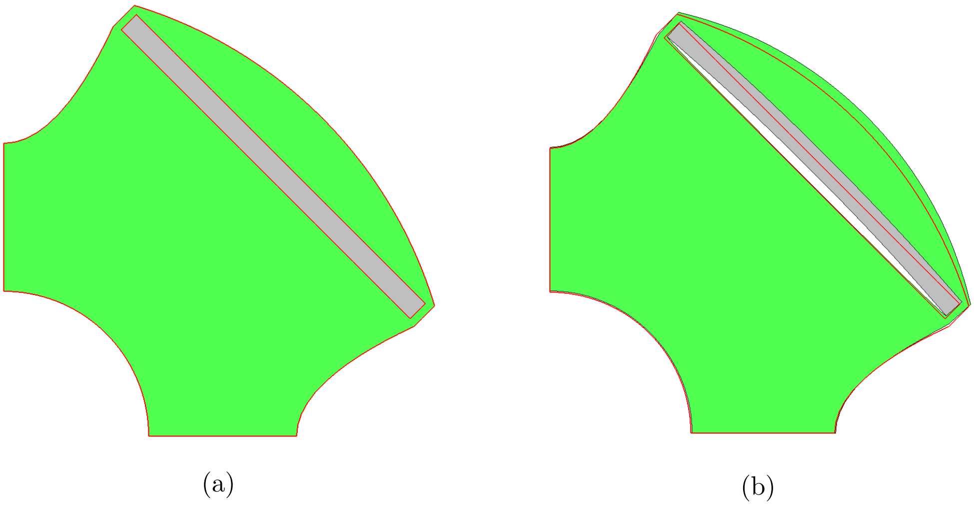
(a) (b)

Figure 4.4: Quarter cross-section of the BR-FI-PM machine's rotor showing (a) the deformation and (b) the deformation scaled by one hundred, at 4800 r/min speed.

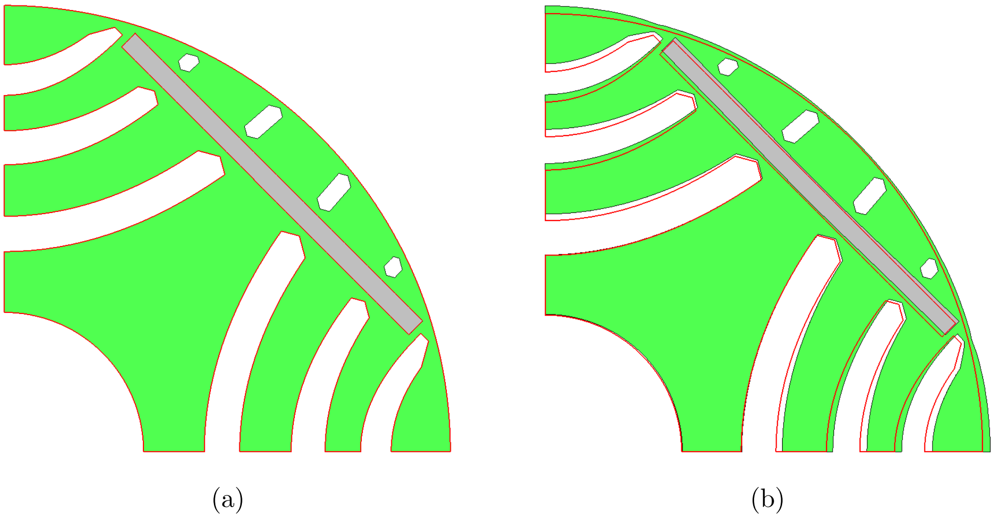

(a) (b)

Figure 4.5: Quarter cross-section of the FBR-FI-PM machine's rotor showing (a) the deformation and (b) the deformation scaled by one hundred, at 4800 r/min speed.

The FBR-FI-PM machine shows a radial displacement of 13 μm at a speed of 4800 r/min. The air-gap is also 0.4 mm and therefore the displacement is deemed acceptable. The deformation is shown in Fig. 4.5a, and is not even visible. In Figure 4.5b the deformation is shown with the displacement scaled by one hundred to show how the rotor deforms.

The deformation of the asymmetric rotors of the BR-FI-PM and FBR-FI-PM machines will be more or less the same as the symmetric rotors and is hence not studied.

4.3 Summary

In this chapter PM demagnetisation and rotor deformation of the optimum designed machines were investigated. The results showed that no demagnetisation occurred in any of the machines for the worst case scenario's given. The PMs of the BR-FI-PM machine only start to show signs of demagnetisation at 340 A, while the PMs of the FBR-FI-PM machine only start to show signs of PM demagnetisation at 390 A. No critical rotor deformation occurred in any of the machines at the maximum speed of 4800 r/min.

Chapter 5

FE and measured results

In this chapter the performance results of the optimised FI-PM machines are presented. Only the asymmetric BR-FI-PM machine is manufactured and tested to validate the results of the FE models.

5.1 FE results of optimum designed machines

Cross-sections of the machines obtained from the design optimisation are shown in Fig. 5.1. The FE results of the rated performance of each machine are given in Table 5.1. The performance of all the machines succeed in the design specifications given in Table 1.1.

From the Table 5.1 note how the asymmetries in the adjacent poles/barriers reduce the torque ripple. The torque waveforms of the symmetric and asymmetric rotors are compared in Figs. 5.2a and 5.2b for the BR-FI-PM and FBR-FI-PM machines respectively. From these results an impressive torque ripple reduction is visible for the BR-FI-PM machine with asymmetric poles, while the FBR-FI-PM machine with asymmetric flux barriers shows also a good reduction in torque ripple. The torque harmonics of the symmetric and asymmetric rotors are compared in Figs. 5.3a and 5.3b for the BR-FI-PM and FBR-FI-PM machines respectively to show which harmonics are reduced by the asymmetry. The dominant torque harmonic orders are $6k$, where $k = 1, 2, 3...n$. From Fig. 5.3 it is evident that the 18th and 12th torque harmonics, amongst others, for the BR-FI-PM and the FBR-FI-PM machine respectively are

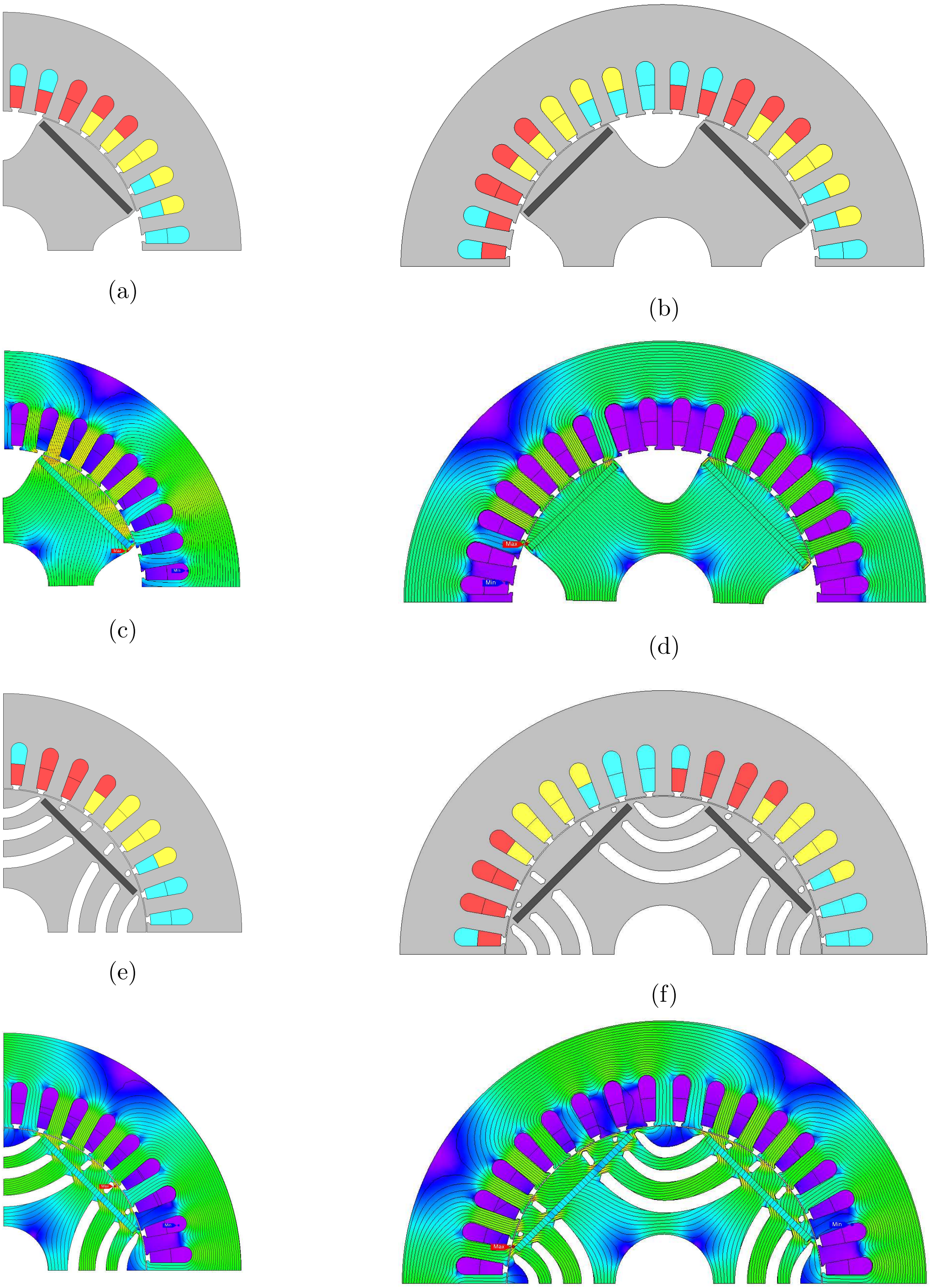

(a) (b) (c) (d) (e) (f) (g) (h)

Figure 5.1: Quarter cross-sections of (a) BR-FI-PM,(b) asymmetric BR-FI-PM, (e) FBR-FI-PM and (f) asymmetric FBR-FI-PM machines, and their field plots in (c), (d), (g) and (h) respectively.

Table 5.1: FE performance results of the optimised machines.

	BR-FI-PM	Asym. BR-FI-PM	FBR-FI-PM	Asym. FBR-FI-PM
Current ($A_{\text{rms phase}}$)	142.78	142.78	132.11	132.11
Current density (A/mm^2)	8.4	8.4	8.4	8.4
Voltage ($V_{\text{rms phase}}$)	123.48	119.79	108.61	110.24
Speed (r/min)	4800	4800	4800	4800
Torque (Nm)	71.53	69.36	71.06	70.1
Torque ripple (%)	39	6.6	10	6.9
Output power (kW)	35.5724	34.8649	35.6646	35.2334
Iron loss (W)	434.32	416.06	364.22	381.4
Copper loss (kW)	1.266	1.266	1.1255	1.1255
Efficiency (%)	95.4	95.39	95.99	95.9
Power Factor	0.696	0.71	0.856	0.834

significantly reduced by the asymmetric rotor configurations. The other performance parameters in Table 5.1 are not affected much by the asymmetry.

As given in Table 5.1 the iron losses for all the machines are approximately a third of the copper loss when using the NO20 lamination steel for the stator and the 50A230 lamination steel for the rotor. The efficiency of all the machines are also very high making it favourable for EV application. Figures 5.4a and 5.4b show the efficiency maps for the asymmetric BR-FI-PM and asymmetric FBR-FI-PM machines respectively over the torque-speed spectrum. The rotational losses, consisting of windage and friction losses, are included in the efficiency calculation. Note how the efficiency increases with speed and torque. With the MG transmission it is possible to operate in the high efficiency region at all time.

Note from Table 5.1 in order to produce an average torque of 70 Nm, the current and voltage of the FBR-FI-PM machines are lower than that of the BR-FI-PM machines for the

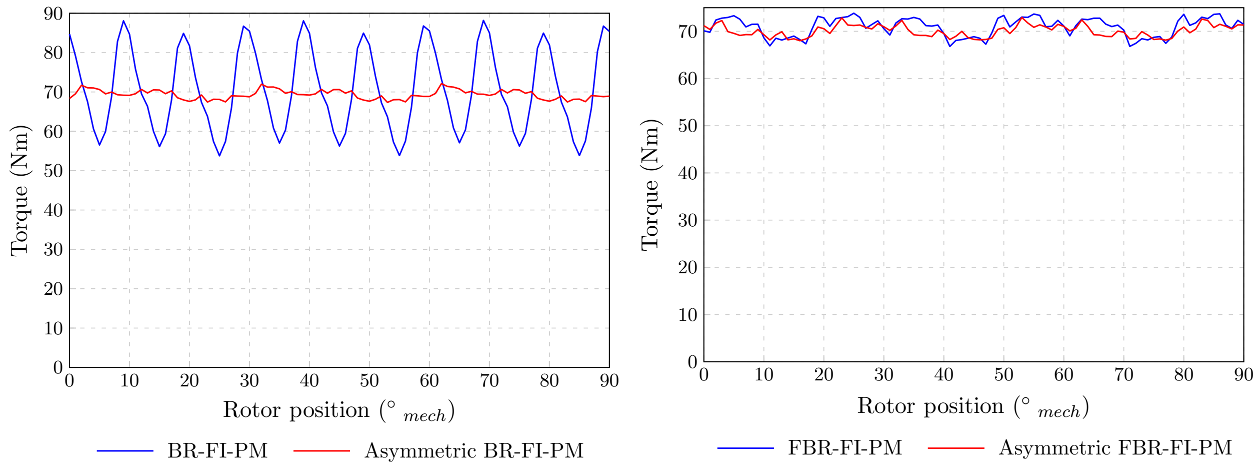

(a) BR-FI-PM machine

(b) FBR-FI-PM machine

Figure 5.2: Torque as a function of rotor position of the FI-PM machines at full load.

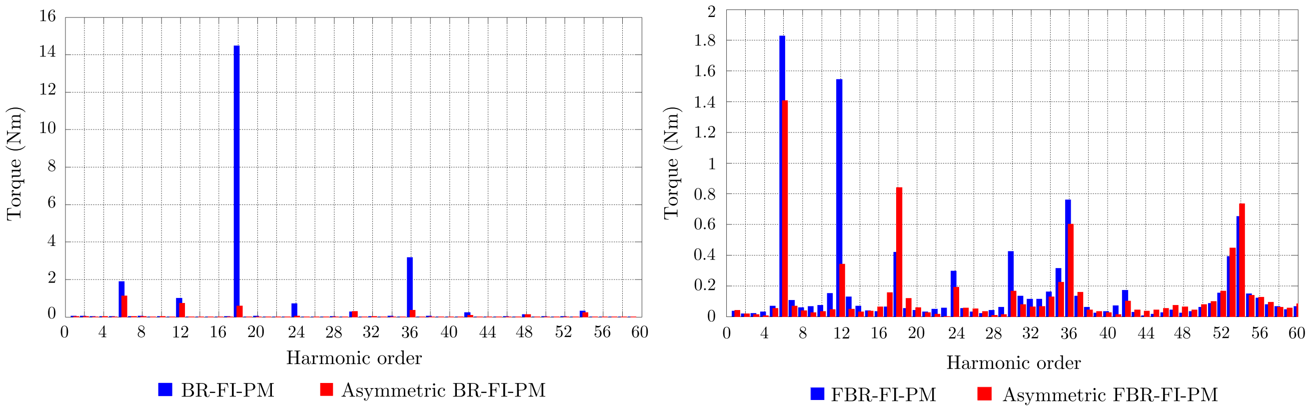

(a) BR-FI-PM machine

(b) FBR-FI-PM machine

Figure 5.3: Full-load torque harmonics of the FI-PM machines.

same current density and turns per slot. This is due to the higher saliency and larger active rotor surface compared to the BR-FI-PM machines. The active rotor surface of the BR-FI-PM machine is smaller than the FBR-FI-PM machines due to the cut-outs across the *q*-axis flux path.

5.2 Measured Results

In order to validate the results obtained from the FE models, tests were conducted in the laboratory and the results are compared to the FE results in this section for the asymmetric

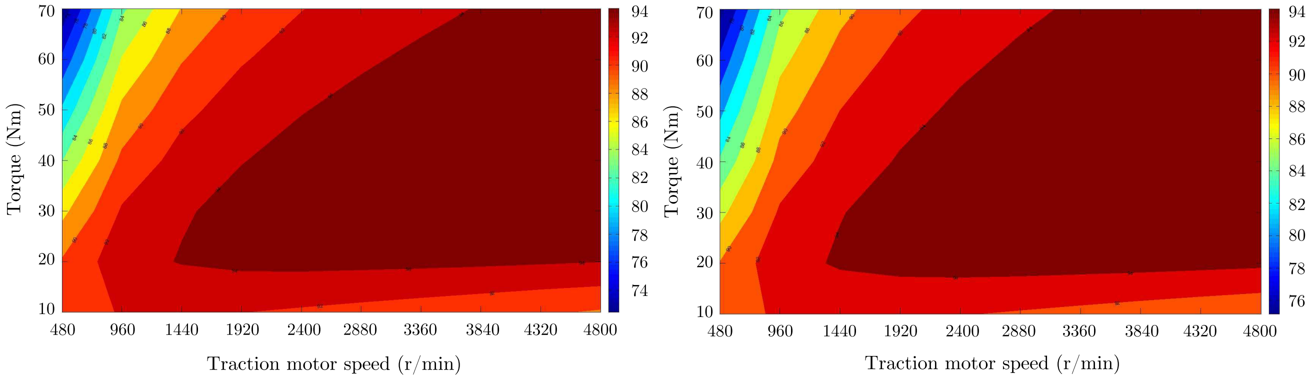

(a)

(b)

Figure 5.4: Efficiency map for (a) asymmetric BR-FI-PM and (b) asymmetric FBR-FI-PM.

BR-FI-PM machine.

5.2.1 Experimental setup

The experimental setup consists of an inverter which drive the BR-FI-PM motor under test, which is connected to a water-cooled eddy-current dynamo meter (dyno) via a torque transducer to measure shaft torque. A diagram of the test setup is shown in Fig. 5.5 with pictures shown in Fig. 5.6. The dyno is used as a load for the FI-PM machine and controlled by supplying DC current to its terminals. The air-cooled FI-PM machine is connected in a Y configuration to the inverter. The inverter is supplied from the grid through a rectifier to its DC bus. A current control scheme is implemented on the Digital Signal Processor (DSP) of the inverter, with a resolver connected to the non drive-end of the BR-FI-PM machine for position feedback to the DSP. Current feedback is obtained via LEM current sensors. With the measurement information available dq PI current controllers are implemented on the DSP to maintain the correct phase currents according to the reference current and the current angle ϕ.

5.2.2 Open-circuit

The open-circuit voltage of the machine is measured by rotating it with another machine at different speeds. The measurements were done at different speed increments up to a speed of 4800 r/min (which would be equal to 126 km/h vehicle speed in 5^{th} gear). The open-circuit calculated FE results were done afterwards at the measured speeds. The measured results are slightly lower than the calculated FE results as shown in Fig. 5.7a. This is due to the the manufacturing tolerances of the PMs. Otherwise, the measured and calculated results show good correlation. The voltage waveform shown in Fig. 5.7b is the result of a measurement at 4687.5 r/min.

Since less PM material is used in FI-PM machines due to the FI operation, the open-circuit voltage is less than in conventional FW-IPM machines. The asymmetric BR-FI-PM machine FE open-circuit voltage at 4800 r/min is 144 V_{rms}, which is below the allowed maximum of 150.0 V_{rms} calculated from the battery pack voltage given in Table 1.1. This is a big advantage over FW-IPM machines as high open-circuit voltages are unwanted in EV drives.

5.2.3 Load

The asymmetric BR-FI-PM machine was tested under steady state load conditions at several load and speed points. A Norma 5000 power analyser was used to measure the input power while the output power is calculated from the measured shaft torque and speed. The shaft torque is measured with a torque sensor, which also measures speed of the machine. The tests were performed at $\frac{1}{4}$, $\frac{2}{4}$, $\frac{3}{4}$ and full load torque with constant current angle. The results of these tests are shown in Fig. 5.8, with the round and filled markers the measured values and the solid lines the FE calculated values. The current magnitudes needed to produce the measured and FE torques in Fig. 5.8, are shown in Fig. 5.9. Note that the measured current is slightly higher than the FE current. This can be described by, amongst other things, the mechanical rotational losses of the test bench that need to be overcome.

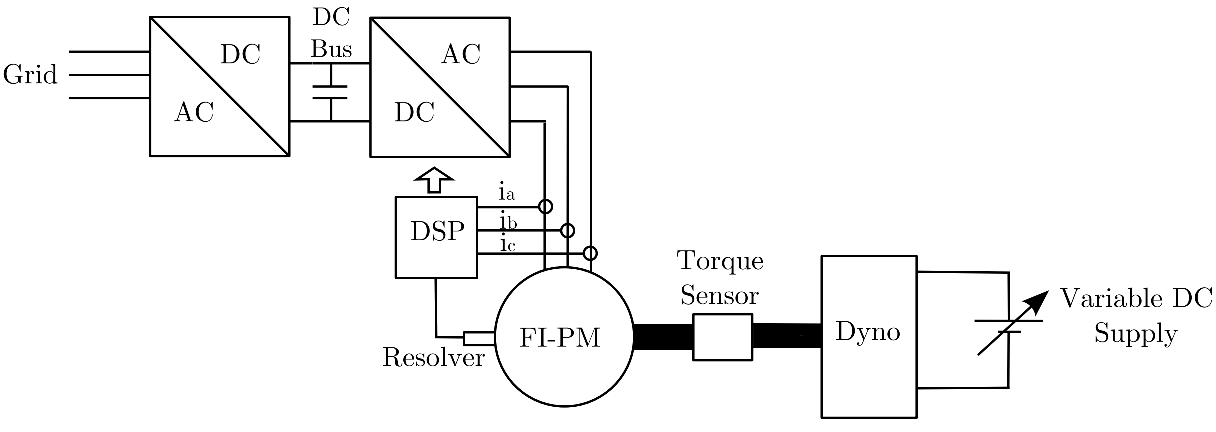

Figure 5.5: Diagram of the test setup.

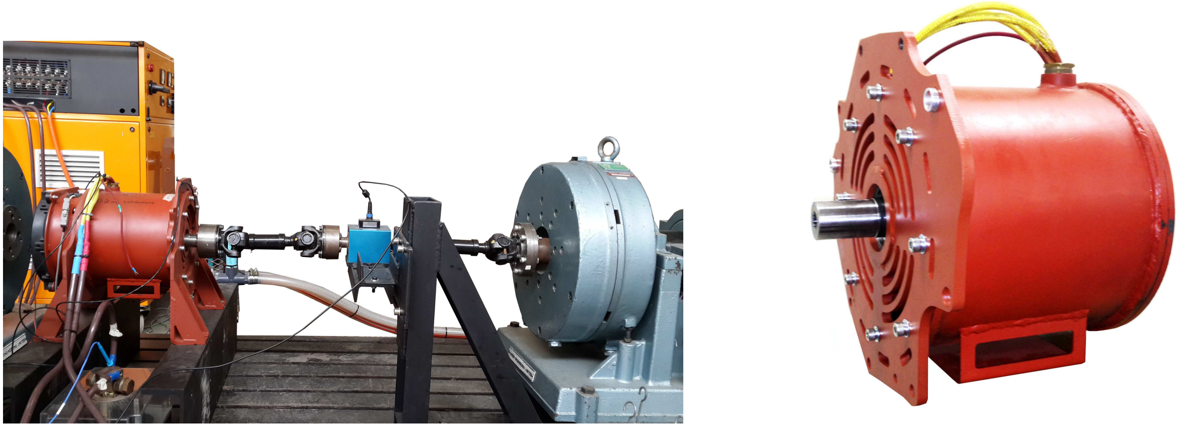

(a) Test bench setup

(b) Asymmetric BR-FI-PM machine

(c) Rotor

(d) Stator

Figure 5.6: Pictures of the test bench setup and machine components.

The measured and calculated efficiencies are shown in Fig. 5.10, with the round filled markers the measured values and the triangular filled markers the FE calculated values. Note that the calculated efficiencies include the mechanical rotational losses of the machine only.

From the load tests it is evident that the measured and FE calculated parameters correlate well, therefore, all other FE calculated results can be deemed accurate. Measurements at high speed and load torque could not be done due to severe mechanical vibration of the test bench at certain speeds.

5.3 Summary

All the designed FI-PM machines met the design specifications. The results showed that the torque ripple is greatly reduced by the asymmetry in the rotor geometries, while other

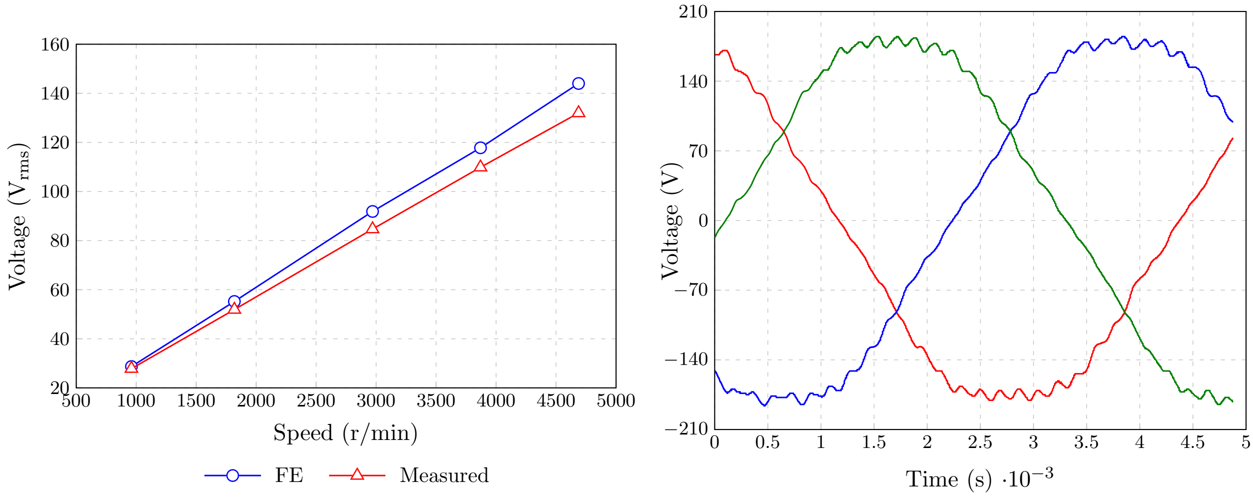

(a)

(b)

Figure 5.7: (a) Measured and calculated open-circuit rms phase voltage. (b) Measured open-circuit phase voltage waveforms at 156.25 Hz (4687.5 r/min).

performance parameters are not affected by the asymmetry. The efficiency of the machines are good making it favourable for EV application. The asymmetric BR-FI-PM machine was manufactured and tested. The measured results correlate well with the FE calculated results to a certain extent.

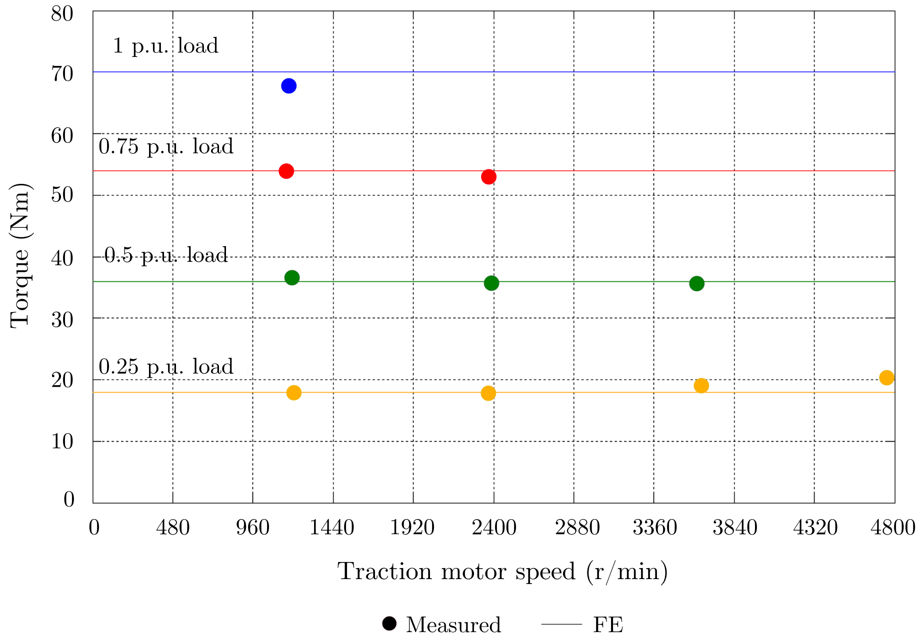

Figure 5.8: Measured and FE calculated torque.

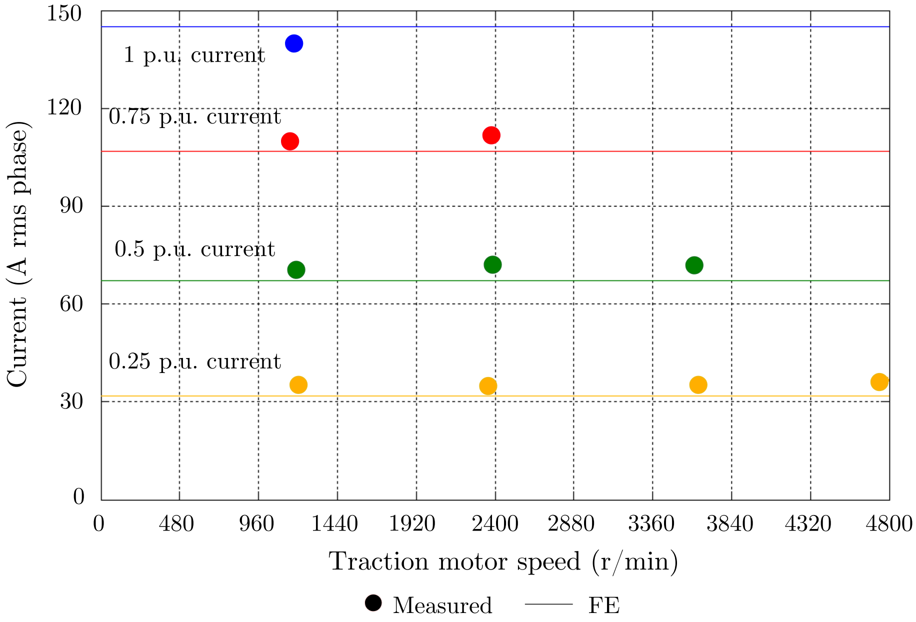

Figure 5.9: Measured and FE calculated current according to the load torque in Fig. 5.8.

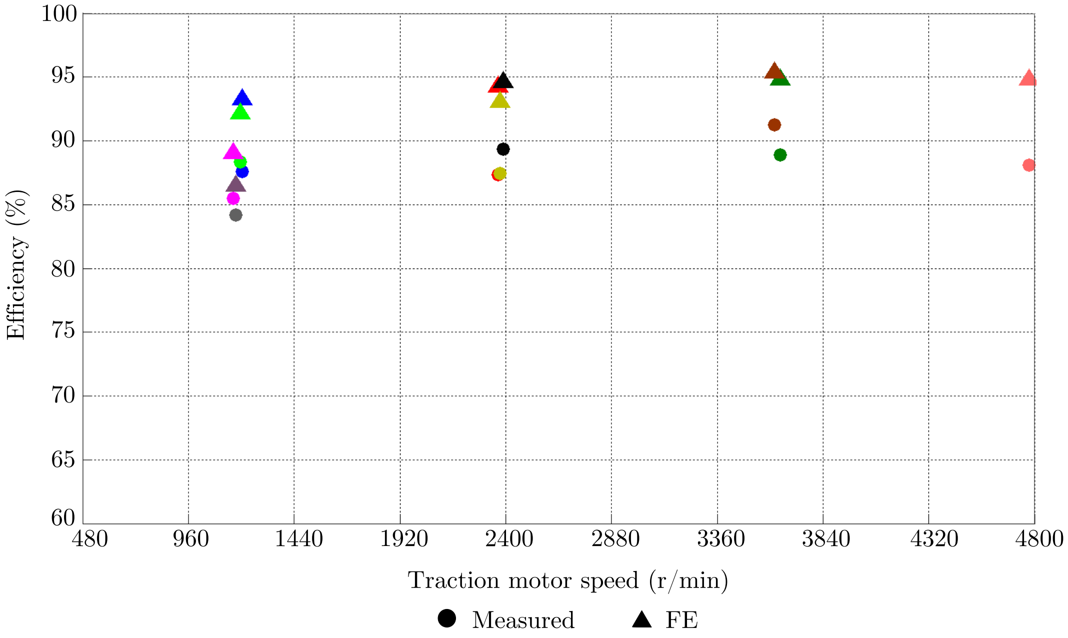

Figure 5.10: Measured and FE calculated efficiency according to the load torque in Fig. 5.8.

Chapter 6

Saliency Performance of the FI-PM machine

To control the FI-PM machines a resolver is needed for position feedback. Position sensors are unwanted in EV's as it introduces a risk of failure, thus, sensorless control schemes, even for a backup, are implemented. In [1] and [10] it is reported that FI-PM machines are well suited for sensorless control. This chapter therefore investigates the position sensorless control capability of the optimised FI-PM machines of Chapter 5. The sensorless control capability of the machine highly depends on the saliency performance. There are two parameters which need to be considered when studying the saliency performance of a machine which are, the saliency ratio and the saliency shift. These two parameters are used to predict the Saliency-Based Position Sensorless Control (SB-PSC) performance of the FI-PM machines by means of FE simulations before the manufacturing process. Larger saliency ratio values are considered better for SB-PSC while the effectiveness of the SB-PSC depends on the saliency shift [39].

6.1 Saliency ratio and -shift

The incremental inductances of a FI-PM machine are defined by

$$L_d = \frac{\partial \lambda_d}{\partial i_d} \quad \text{and} \tag{6.1}$$

$$L_q = \frac{\partial \lambda_q}{\partial i_q}. \tag{6.2}$$

These inductances vary with i_d and i_q as $\lambda_d = f(i_d, i_q)$ and $\lambda_q = f(i_d, i_q)$ [40]. The mutual inductances, caused by cross-saturation, can be assumed to be equal and are given by [41]

$$\frac{\partial \lambda_d}{\partial i_d} = \frac{\partial \lambda_q}{\partial i_q} = L_{dq} = L_{qd}. \tag{6.3}$$

The mutual inductance L_{dq} causes the magnetic axis to shift away from the rotor d-axis by an angle φ. This angular offset is known as the saliency shift and is given by [40, 41]

$$\varphi = -0.5arctan\left(\frac{L_{dq}}{\Delta L}\right), \tag{6.4}$$

where $\Delta L = (L_q - L_d)/2$. The saliency shift is zero at no-load or if the geometric saliency masks the effect of a saturation based saliency and prevent the magnetic axis from shifting away from the rotor d-axis [40]. The saliency ratio is given as in (6.5) with its magnitude within the range of 0 to 1. [40, 41].

$$\xi = \frac{\sqrt{(L_d - L_q)^2 + 4L_{dq}^2}}{L_d + L_q} \tag{6.5}$$

From (6.5) it is evident that the mutual inductance L_{dq} also contributes to the saliency ratio magnitude.

6.2 Saliency performance comparison

The optimised FI-PM machines in Chapter 5 are compared in terms of their saliency ratio and -shift. A large saliency ratio is desired for SB-PSC while a small saliency shift is desired. It is also desirable that the saliency ratio increase linearly with increasing load. This is advantageous for sensorless control as it makes the control less complex and improves reliability [1].

The FE calculated saliency ratio and -shift results versus current are shown in Figs. 6.1a and 6.1b respectively. The BR-FI-PM has a slightly higher saliency ratio than the FBR-FI-PM machine, however, the saliency shift of the FBR-FI-PM machine is much lower than the BR-FI-PM machine as shown in Fig. 6.1. The lower saliency shift of the FBR-FI-PM machine

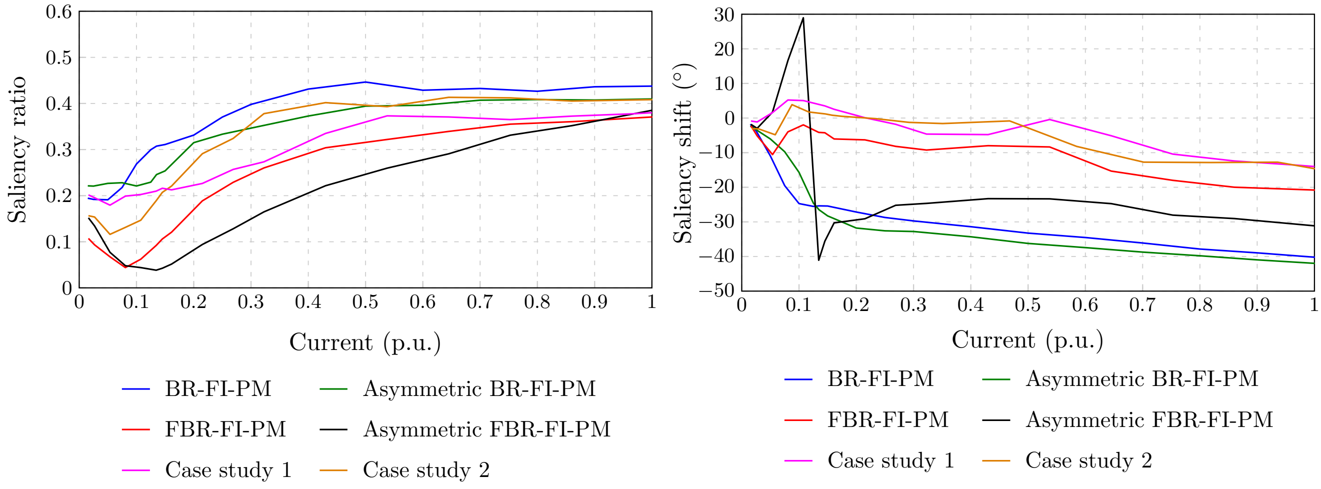

(a)

(b)

Figure 6.1: (a) FE calculated saliency ratio. (b) FE calculated saliency shift.

is due its lower mutual inductance compared to the BR-FI-PM machine shown in Fig. 6.2. The mutual inductance in the FBR-FI-PM machine is lower due to the flux barriers which constraints the flux within definite paths, thus reducing cross-coupling. The asymmetric BR-FI-PM machine has a lower saliency ratio and -shift than its symmetric counterpart. From their respective mutual inductances shown in Fig. 6.2, it is evident that the asymmetry in the rotor produces more cross-coupling [43,44]. This is also true for the asymmetric FBR-FI-PM and its symmetric counterpart. In Fig. 6.1b it is shown that the sign of the saliency shift of the asymmetric FBR-FI-PM machine changes when the gradient of the saliency ratio changes direction at 0.1 $p.u.$.

From Fig. 6.1a it is evident that the saliency ratios of all the FI-PM machines increase linearly with load current. In this regard the FI-PM machine is superior to RSM's and FW-IPM machines as these machine's saliency ratios decrease with increasing load current [39].

A case study was conducted where the iron ribs of the FBR-FI-PM machine at the rotor surface was removed. This was done to reduce the amount of leakage flux paths in the machine which increases cross-coupling, thus, increase the saliency shift. The machine geometry with the removed iron ribs at the rotor surface is shown in Fig. 6.3. Note the slot openings at the rotor surface where the iron ribs are removed compared to FBR-FI-PM machine in Fig. 3.4a. The results obtained for the saliency ratio and -shift are added in Figs. 6.1a and 6.1b,

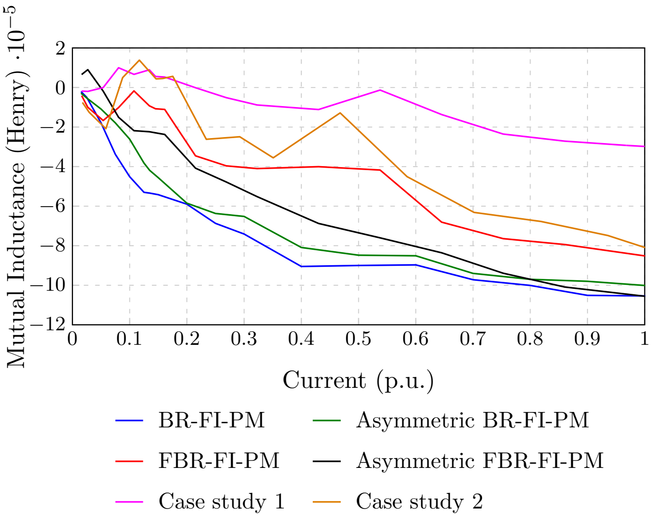

Figure 6.2: Mutual inductances.

labelled as Case study 1. These results show a very good improvement in saliency shift while the saliency ratio is slightly improved from the original FBR-FI-PM machine. The cross-coupling in the machine reduced significantly and therefore the mutual inductance shown in Fig. 6.2. The torque ripple, however, of this machine increased a lot with the iron ribs removed.

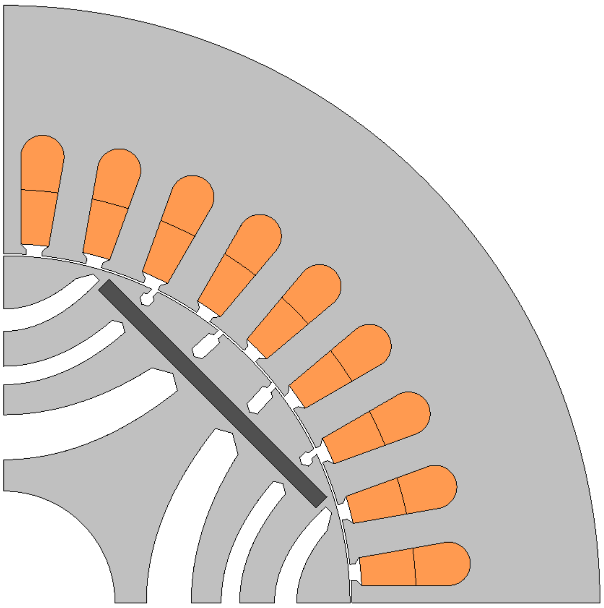

Figure 6.3: The FI-PM machine of case study 1.

Another case study was conducted where the FBR-FI-PM machine was optimised for saliency shift. The results obtained for the saliency ratio and -shift are also added in Figs. 6.1a and 6.1b, labelled as Case study 2. It is very difficult to optimise for saliency shift i.e cross-coupling as the average torque of the machine reduces [44]. From the results it is evident that the saliency shift and -ratio improved for the machine optimised for saliency ratio compared to the FBR-FI-PM optimised for $\frac{P_{cu}}{T_{avg}}$. The saliency shift is more or less the same as for the machine in Case study 1 which exhibit a high torque ripple. From Fig. 6.2 it is evident that the cross-coupling is less for this machine compared the original FBR-FI-PM machine. The machine from Case study 1, however, shows the least cross-coupling.

6.3 Summary

In this chapter the saliency performance of the optimum designed machines of the previous chapter was evaluated. The saliency ratio of the FI-PM machines increased linearly with load which hold advantages for SB-PSC. The asymmetric rotor topologies introduced a larger mutual inductance compared to their symmetric counterparts, thus higher cross-coupling is present in these rotors and therefore a higher saliency shift. A case study was conducted where the iron ribs at the rotor surface of the FBR-FI-PM machine was removed to reduce leakage flux paths. The results showed a significant reduction in mutual inductance and therefore in saliency shift compared to the original FBR-FI-PM machine. The the torque ripple, however, increased. Another case study was conducted where the FBR-FI-PM machine was optimised for saliency shift. The results showed an increase in saliency shift and -ratio compared to the original FBR-FI-PM machine.

Chapter 7

Conclusions

The work in this thesis is about the optimal design of FI-PM machines for the use with a MG transmission drive-train for EVs. The FI-PM machines are designed according to tractive effort specifications of the Opel Corsa 1.4i Lite vehicle. All the machines performed well considering the volumetric space available and the required torque and power specifications. In this chapter the findings of the work is highlighted.

7.1 Design optimisation

- A gradient-based optimisation algorithm was used and very good results were obtained.
- A BR-FI-PM machine was designed with the focus to reduce expensive PM volume. Good results were obtained from the optimisation and the PM height was reduced by the optimisation algorithm beyond manufacturing capabilities, therefore, needed to be kept at a minimum. The BR-FI-PM machine had only a few design variables and therefore reduced computation time to optimise the machine design optimisation.
- Another FI-PM machine, called FBR-FI-PM machine, was designed which contained internal rotor flux barriers with the objective function being the $\frac{P_{cu}}{T_{avg}}$. The FBR-FI-PM machine generates more reluctance torque than the BR-FI-PM machine due to the internal rotor flux barriers, thus, the stack length decreased by 15.7 % from the BR-FI-PM machine. The PM volume decreased by 15.3% from what is used in the BR-FI-PM machine. The reduction in stack length and PM volume reduced the overall cost of the machine.

- Both machines exhibit a high torque ripple, but a new topology was implemented where adjacent rotor poles/barriers are asymmetric to reduce torque ripple. The asymmetric poles/barriers proved to be effective for torque ripple reduction below 7%, and can thus be used as an alternative for rotor stack skewing.

7.2 PM demagnetisation and rotor deformation

- A PM demagnetisation study was conducted on the optimum designed machines of Chapter 3. At a worst case scenario condition of 320 A and 120 $^{\circ}C$, no signs of PM demagnetisation was visible on the PM surfaces. It was found that the PMs of the BR-FI-PM machine only start to show signs of demagnetisation at 340 A, while the PMs of the FBR-FI-PM machine only start to show signs of PM demagnetisation at 390 A at a temperature of 120 $^{\circ}C$.
- A study was conducted on how the rotors of the optimum designed machines deform due to centrifugal forces, at a maximum speed of 4800 r/min. The results showed that a radial displacement of 16 μm occur for the BR-FI-PM rotor while a radial displacement of 13 μm occur for the FBR-FI-PM rotor. These displacements are well below the air-gap length of 0.4 mm and are therefore deemed acceptable.

7.3 Optimum designed machines

- The optimum designed FI-PM machines showed very good efficiency, especially in the higher speed and load region, making it favourable for EV application.
- The open-circuit tests conducted showed that the back-EMF is below the allowed maximum of 150 V_{rms}.
- The load tests conducted correlates well with the FE calculated results, therefore the FE simulations is deemed accurate.

7.4 Saliency performance

- The saliency ratio of the optimum designed machines showed a linear increase with load making them favourable for SB-PSC.

- The asymmetric rotor topologies introduced a larger mutual inductance compared to their symmetric counterparts, therefore higher cross-coupling and saliency shift.
- A case study was done were the iron ribs at the rotor surface of the FBR-FI-PM machine was removed to reduce the leakage flux paths. The results showed a big reduction in mutual inductance and therefore in saliency shift. The torque ripple, however, increased.
- Another case study was done where the original FBR-FI-PM machine was optimised for saliency shift. The results showed a very good increase in saliency shift and -ratio.

7.5 Recommendations for future work

From the work in this thesis on FI-PM machines the following recommendations are made for further study and investigation:

- The FI-PM machines need to be optimised using low-coercive force PMs to even further reduce cost by eliminating rare earth materials. The volume of low-coercive force PMs needed to obtain the same performance as a machine with rare earth PMs, must be compared.
- The FI-PM machines need to be tested with SB-PSC in order to verify if the saliency performance reflect the machine's sensorless control capability.

References

[1] N. Limsuwan, Y. Shibukawa, D.D. Reigosa, and R.D. Lorenz. Novel design of flux-intensifying interior permanent magnet synchronous machine suitable for self-sensing control at very low speed and power conversion. *Industry Applications, IEEE Transactions on*, 47(5):2004 –2012, Sept.-Oct. 2011.

[2] N. Bianchi and S. Bolognani. Performance analysis of an ipm motor with segmented rotor for flux-weakening applications. In *Electrical Machines and Drives, 1999. Ninth International Conference on (Conf. Publ. No. 468)*, pages 49–53, 1999.

[3] N. Bianchi, S. Bolognani, and B.J. Chalmers. Salient-rotor pm synchronous motors for an extended flux-weakening operation range. *Industry Applications, IEEE Transactions on*, 36(4):1118–1125, 2000.

[4] A. Akatsu, M. Arimitsu, and S. Wakui. Design and control of field intensified interior permanent magnet synchronous machine. *IEEJ Transactions on Industry Applications*, 126(7):827–834, 2006.

[5] Shanshan Wu, D.D. Reigosa, Y. Shibukawa, M.A. Leetmaa, R.D. Lorenz, and Yongdong Li. Interior permanent-magnet synchronous motor design for improving self-sensing performance at very low speed. *Industry Applications, IEEE Transactions on*, 45(6):1939 –1946, Nov.-Dec. 2009.

[6] N. Bianchi and S. Bolognani. Influence of rotor geometry of an ipm motor on sensorless control feasibility. *Industry Applications, IEEE Transactions on*, 43(1):87–96, 2007.

[7] N. Bianchi, S. Bolognani, and M. Zigliotto. Design hints of an ipm synchronous motor for an effective position sensorless control. In *Power Electronics Specialists Conference, 2005. PESC '05. IEEE 36th*, pages 1560–1566, 2005.

[8] D.D. Reigosa, K. Akatsu, N. Limsuwan, Y. Shibukawa, and R.D. Lorenz. Self-sensing comparison of fractional slot pitch winding versus distributed winding for fw- and fi-ipmsms based on carrier signal injection at very low speed. *Industry Applications, IEEE Transactions on*, 46(6):2467–2474, 2010.

[9] T. Kato, N. Limsuwan, ChenYen Yu, K. Akatsu, and R.D. Lorenz. Rare earth reduction using a novel variable magnetomotive force, flux intensified ipm machine. In *Energy Conversion Congress and Exposition (ECCE), 2012 IEEE*, pages 4346–4353, 2012.

[10] N. Limsuwan, T. Kato, K. Akatsu, and R.D. Lorenz. Design and evaluation of a variable-flux flux-intensifying interior permanent magnet machine. In *Energy Conversion Congress and Exposition (ECCE), 2012 IEEE*, pages 3670–3677, 2012.

[11] Chen-Yen Yu, J. Tamura, D.D. Reigosa, and R.D. Lorenz. Position self-sensing evaluation of a fi-ipmsm based on high-frequency signal injection methods. *Industry Applications, IEEE Transactions on*, 49(2):880–888, 2013.

[12] Q. Ren, D.A. Crolla, and A. Morris. Effect of transmission design on electric vehicle (ev) performance. In *Vehicle Power and Propulsion Conference, 2009. VPPC '09. IEEE*, pages 1260 –1265, sept. 2009.

[13] D. Paul. Multi-speed transmissions for electric vehicle applications. Technical report, Antov Automotive Technologies Ltd, Sept. 2011.

[14] A. Sorniotti, M. Boscolo, A. Turner, and C. Cavallino. Optimization of a multi-speed electric axle as a function of the electric motor properties. In *Vehicle Power and Propulsion Conference (VPPC), 2010 IEEE*, pages 1 –6, Sept. 2010.

[15] Lin Lai and M. Ehsani. Sensitivity analysis of vehicle performance to transmission parameters in parallel hevs with dynamic programming optimization. In *Transportation Electrification Conference and Expo (ITEC), 2012 IEEE*, pages 1 –5, June 2012.

[16] T. Hofman and C.H. Dai. Energy efficiency analysis and comparison of transmission technologies for an electric vehicle. In *Vehicle Power and Propulsion Conference (VPPC), 2010 IEEE*, pages 1 –6, Sept. 2010.

[17] M. Ehsani, Y. Gao, and A. Emadi. *Modern Electric, Hybrid Electric, and Fuel Cell Vehicles: Fundamentals, Theory, and Design.* CRC Press, second edition, 2010.

[18] L. Lai and M. Ehsani. Sensitivity analysis of vehicle performance to transmission parameters in parallel hevs with dynamic programming optimization. In *Transportation Electrification Conference and Expo (ITEC), 2012 IEEE*, pages 1 –5, June 2012.

[19] S. Roberts. Multi-speed transmissions for electric vehicle applications. *ATZ Worldwide*, 114(4):8–11, 2012.

[20] H.W. De Kock. Dynamic control of the permanent magnet assisted reluctance synchronous machine with constant current angle. Master's thesis, University of Stellenbosch, 2006.

[21] A.J. Rix. *Design, Comparison and Experimental Evaluation of Non-Overlap Winding Radial Flux Permanent Magnet Hub Drives for Electric Vehicles.* PhD thesis, Stellenbosch University, March 2011.

[22] M.J. Kamper and F.S. Van der Merwe. *Design optimisation of cageless flux barrier rotor reluctance synchronous machine.* PhD thesis, University of Stellenbosch, December 1996.

[23] M.J. Kamper. Design of a pm reluctance machine. Technical report, Stellenbosch University, 2009.

[24] M.H.A. Prins. A performance study of reluctance synchronous machines fed by non sinusoidal currents. Master's thesis, Cape Peninsula University of Technology, 2011.

[25] Michiel H.A. Prins, Chris W. Vorster, and Maarten J. Kamper. Reluctance synchronous and field intensified-pm motors for variable-gear electric vehicle drives. In *Energy Conversion Congress and Exposition (ECCE), 2013 IEEE*, pages 657–664, 2013.

[26] J.F. Gieras and M. Wing. *Permanent Magnet Motor Technology: Design and Applications, Second Edition,.* Electrical and Computer Engineering. Taylor & Francis, 2002.

[27] G.N. Vanderplaats. *Numerical Optimization Techniques for Engineering Design.* Mcgraw Hill, 4th edition, 2005.

[28] G. Venter. "Review of Optimization Techniques," in *Encyclopedia of Aerospace Engineering.* Wiley and Sons, 2010.

[29] X.B. Bomela and M.J. Kamper. Effect of stator chording and rotor skewing on performance of reluctance synchronous machine. *Industry Applications, IEEE Transactions on*, 38(1):91–100, 2002.

[30] R.D. Lorenz, N. Limsuwan, Y. Shibukawa, and D.D. Reigosa. Novel design of flux-intensifying interior permanent magnet synchronous machine suitable for self-sensing control at very low speed and power conversion. *IEEE Transactions on Industry Applications*, 47(5):2004–2012, 2011.

[31] N. Limsuwan, T. Kato, and R.D. Lorenz. Concurrent design of interior-permanent-magnet machines for self-sensing and power conversion. *Industry Applications, IEEE Transactions on*, 48(6):2157–2164, 2012.

[32] A. Vagati, M. Pastorelli, G. Francheschini, and S.C. Petrache. Design of low-torque-ripple synchronous reluctance motors. *Industry Applications, IEEE Transactions on*, 34(4):758–765, 1998.

[33] M. Sanada, K. Hiramoto, S. Morimoto, and Y. Takeda. Torque ripple improvement for synchronous reluctance motor using an asymmetric flux barrier arrangement. *Industry Applications, IEEE Transactions on*, 40(4):1076–1082, 2004.

[34] N. Bianchi, S. Bolognani, D. Bon, and M.D. Pre. Rotor flux-barrier design for torque ripple reduction in synchronous reluctance and pm-assisted synchronous reluctance motors. *Industry Applications, IEEE Transactions on*, 45(3):921–928, 2009.

[35] P. Alotto, M. Barcaro, N. Bianchi, and M. Guarnieri. Optimization of interior pm motors with machaon rotor flux barriers. *Magnetics, IEEE Transactions on*, 47(5):958–961, 2011.

[36] L. Alberti, M. Barcaro, and N. Bianchi. Design of a low torque ripple fractional-slot interior permanent magnet motor. In *Energy Conversion Congress and Exposition (ECCE), 2012 IEEE*, pages 509–516, 2012.

[37] J. Zhao, M.J. Kamper, and F.S. Van der Merwe. On-line control method to reduce mechanical vibration and torque ripple in reluctance synchronous machine drives. In

Industrial Electronics, Control and Instrumentation, 1997. IECON 97. 23rd International Conference on, volume 1, pages 126–131 vol.1, 1997.

[38] H.C. Seherr-Thoss, F. Schmelz, and E. Aucktor. *Universal Joints and Driveshafts: Analysis, Design, Applications.* Springer, 2006.

[39] W.T. Villet, M.H.A Prins, C.W. Vorster, and M.J. Kamper. Saliency performance investigation of synchronous machines for position sensorless controlled ev drives. In *Symposium on Sensorless Control for Electrical Drives. In proceeding of*, volume 4, 2013.

[40] T. Frenzke. Impacts of cross-saturation on sensorless control of surface permanent magnet synchronous motors. In *Power Electronics and Applications, 2005 European Conference on*, pages 10 pp.–P.10, 2005.

[41] P. Guglielmi, M. Pastorelli, and A. Vagati. Cross-saturation effects in ipm motors and related impact on sensorless control. *Industry Applications, IEEE Transactions on*, 42(6):1516–1522, 2006.

[42] Shanshan Wu, D.D. Reigosa, Y. Shibukawa, M.A. Leetmaa, R.D. Lorenz, and Yongdong Li. Interior permanent-magnet synchronous motor design for improving self-sensing performance at very low speed. *Industry Applications, IEEE Transactions on*, 45(6):1939–1946, 2009.

[43] N. Bianchi, S. Bolognani, and M. Zigliotto. Design hints of an ipm synchronous motor for an effective position sensorless control. In *Power Electronics Specialists Conference, 2005. PESC '05. IEEE 36th*, pages 1560–1566, 2005.

[44] N. Bianchi and S. Bolognani. Influence of rotor geometry of an ipm motor on sensorless control feasibility. *Industry Applications, IEEE Transactions on*, 43(1):87–96, 2007.